



The Role of Proton Cyclotron Resonance as a Dissipation Mechanism in Solar Wind Turbulence: A Statistical Study at Ion-kinetic Scales

Lloyd D. Woodham¹ , Robert T. Wicks^{1,2} , Daniel Verscharen^{1,3} , and Christopher J. Owen¹ ¹ Mullard Space Science Laboratory, University College London, Holmbury St. Mary, Dorking, Surrey RH5 6NT, UK; woodhamlloyd@gmail.com² Institute for Risk and Disaster Reduction, University College London, Gower Street, London WC1E 6BT, UK³ Space Science Center, University of New Hampshire, Durham, NH 03824, USA

Received 2018 January 9; revised 2018 February 7; accepted 2018 February 14; published 2018 March 23

Abstract

We use magnetic field and ion moment data from the MFI and SWE instruments on board the *Wind* spacecraft to study the nature of solar wind turbulence at ion-kinetic scales. We analyze the spectral properties of magnetic field fluctuations between 0.1 and 5.4 Hz during 2012 using an automated routine, computing high-resolution 92 s power and magnetic helicity spectra. To ensure the spectral features are physical, we make the first in-flight measurement of the MFI “noise-floor” using tail-lobe crossings of the Earth’s magnetosphere during early 2004. We utilize Taylor’s hypothesis to Doppler-shift into the spacecraft frequency frame, finding that the spectral break observed at these frequencies is best associated with the proton cyclotron resonance scale, $1/k_c$, rather than the proton inertial length, d_i , or proton gyroscale, ρ_i . This agreement is strongest when we consider periods where $\beta_{i,\perp} \sim 1$, and is consistent with a spectral break at d_i for $\beta_{i,\perp} \ll 1$ and at ρ_i for $\beta_{i,\perp} \gg 1$. We also find that the coherent magnetic helicity signature observed at these frequencies is bounded at low frequencies by $1/k_c$, and its absolute value reaches a maximum at ρ_i . These results hold in both slow and fast wind streams, but with a better correlation in the more Alfvénic fast wind where the helicity signature is strongest. We conclude that these findings are consistent with proton cyclotron resonance as an important mechanism for dissipation of turbulent energy in the solar wind, occurring at least half the time in our selected interval. However, we do not rule out additional mechanisms.

Key words: plasmas – solar wind – Sun: heliosphere – turbulence – waves

Supporting material: data behind figure

1. Introduction

The solar wind supports a turbulent energy cascade where the spectrum of magnetic field fluctuations follows a Kolmogorov inertial range scaling of $k^{-5/3}$ extending over several decades (Goldstein et al. 1995; Tu & Marsch 1995; Bruno & Carbone 2013). We can convert the wavenumber, k , of the turbulent fluctuations along the sampling direction of the solar wind flow to a frequency, f , using Taylor’s hypothesis (Taylor 1938): $f \sim kv_{sw}/2\pi$, where v_{sw} is the solar wind speed. At frequencies in the plasma frame of the order of the ion gyrofrequency, $\Omega_i = q_i B_0/m_i$, typically measured around 0.1–1 Hz in the spacecraft frame at 1 au, the spectrum steepens (e.g., Coleman 1968; Russell 1972). Here, q_i is the ion charge, m_i is the ion mass, and B_0 is the background field strength. The observed spectral break in the power spectra at these so-called ion-kinetic frequencies has been attributed to the onset of kinetic effects such as dispersion or turbulent dissipation (see Alexandrova et al. 2013; Kiyani et al. 2015; Chen 2016, and references therein), although the actual physical mechanisms behind the steepening remain poorly understood.

In situ data from spacecraft have revealed a bimodal distribution in solar wind speed with two distinct peaks, leading to the designation of two types of wind: slow ($\sim 350 \text{ km s}^{-1}$) and fast ($\sim 600 \text{ km s}^{-1}$), attributed to different source regions in the solar corona (e.g., Schwenn 1990; Habbal

et al. 1997). In fast wind streams, the spectral steepening is sometimes associated with the start of a variable transition range spanning less than a decade in frequency (Sahraoui et al. 2010; Smith et al. 2012; Kiyani et al. 2013; Bruno et al. 2014, 2017, see also the power spectra in Kiyani et al. 2009; Chen et al. 2010b). The spectral index in this range typically lies between -2 and -4 (Smith et al. 2006; Hamilton et al. 2008; Koval & Szabo 2013; Bruno et al. 2014). At even higher frequencies, the spectrum changes again to a second, more “universal” power law of $f^{-2.8}$ continuing toward electron scales, associated with dispersive modes such as kinetic Alfvén waves (hereafter, KAWs) and whistler waves (e.g., Gary & Smith 2009; TenBarge et al. 2012; Boldyrev et al. 2013), or small-scale coherent structures such as current sheets (e.g., Perri et al. 2012). The slow wind in general typically lacks a transition range and instead shows a single steepening from $f^{-5/3}$ to about $f^{-2.8}$ (Bruno et al. 2014, 2017).

There is strong evidence of the coupling between magnetic energy in the turbulent fluctuations and kinetic energy of the ions, linking the large-scale turbulent cascade with heating of the solar wind particle distributions. For example, the temperature of the solar wind decreases with radial distance more slowly than expected for adiabatic expansion (Marsch et al. 1982b; Richardson et al. 1995), implying an active heating process during its expansion (e.g., Cranmer et al. 2009), which is consistent with the energy cascade rate throughout the inertial range (e.g., MacBride et al. 2008; Stawarz et al. 2009). In the fast wind, the temperature anisotropy, T_{\perp}/T_{\parallel} , of the proton core population and plateau formation in the proton velocity distributions (Marsch & Tu

2001; Tu & Marsch 2001, 2002; Marsch et al. 2004; Heuer & Marsch 2007) also suggest on-going heating by the turbulent cascade. These observations indicate that dissipation of the turbulent fluctuations is a likely candidate for the spectral steepening. In fact, the steepness of spectra is correlated with the energy cascade rate and power level in the inertial range (Smith et al. 2006; Bruno et al. 2014), as well as the thermal proton temperature (Leamon et al. 1998b), implying that steeper slopes are associated with greater heating rates.

The kinetic features of the proton velocity distributions highlight a deviation from local thermal equilibrium that is due to the lack of Coulomb collisions in the solar wind (Marsch 2012, see also the review by Marsch 2006). Instead, these features are likely regulated by linear and nonlinear wave-particle interactions (e.g., Howes et al. 2008a; Schekochihin et al. 2009; Chandran et al. 2010; Smith et al. 2012; Osman et al. 2014) such as ion cyclotron resonance, Landau resonance and transit-time damping, stochastic heating, entropy cascades, and mechanisms associated with reconnection. There is also evidence that plasma instabilities play an important role (Kasper et al. 2002; Hellinger et al. 2006; Matteini et al. 2007; Bale et al. 2009; Maruca et al. 2012; Osman et al. 2013; Servidio et al. 2014). These physical processes may lead to the dissipation of energy from the turbulence and subsequent heating of ions observed by spacecraft. Understanding these mechanisms in the collisionless solar wind plasma is a major outstanding problem in the field of heliophysics research.

1.1. Spectral Steepening at High Frequencies

Several different characteristic ion plasma scales have been suggested to correspond to the observed spectral steepening, and each one is associated with a different plasma heating process. Two scales that are commonly proposed to correspond to the spectral break are the ion inertial length, $d_i = v_A/\Omega_i$, and the ion gyroscale, $\rho_i = v_{th,\perp}/\Omega_i$. Here, $v_A = B_0/\sqrt{\mu_0 n_i m_i}$ is the Alfvén speed, n_i is the ion number density, $v_{th,\perp} = \sqrt{2k_B T_{i,\perp}/m_i}$ is the ion thermal speed perpendicular to the background magnetic field, B_0 , and $T_{i,\perp}$ is the ion perpendicular temperature. The inertial length is associated with the onset of dispersive effects due to the Hall current term, as well as reconnection of small-scale current sheets (Dmitruk et al. 2004; Galtier 2006; Galtier & Buchlin 2007), whereas the transition from Alfvén wave to KAW-dominated turbulence occurs at scales comparable to the gyroscale (Howes et al. 2008a; Schekochihin et al. 2009; Boldyrev & Perez 2012).

Another explanation for the observed spectral steepening is cyclotron resonance of Alfvén waves with solar wind ions (e.g., Coleman 1968; Marsch et al. 1982a, 2003; Denskat et al. 1983; Goldstein et al. 1994; Gary & Borovsky 2004; Smith et al. 2012). Here, the only ions we consider are protons, and throughout this paper we use the subscript i to refer exclusively to protons. Leamon et al. (1998b) proposed a wavenumber for the onset of cyclotron damping of Alfvén waves (see also Gary 1999). The cyclotron resonance condition for protons is given by equating the Doppler-shifted wave frequency in the plasma frame, ω , to the proton gyrofrequency, Ω_i (e.g., see Stix 1992),

$$\omega(k_{\parallel}) - k_{\parallel}v_{\parallel} = \pm\Omega_i, \quad (1)$$

where v_{\parallel} is the parallel velocity of the resonant protons and k_{\parallel} is the parallel component of the wavenumber with respect to B_0 .

The \pm sign takes into account the sense of polarization of the wave. The wave electric field vector of left-hand circularly polarized Alfvén/ion-cyclotron waves (hereafter, AICs) propagating parallel to B_0 rotates in the same direction as proton gyration, so we use the positive sign. This interaction is most effective if $k_{\parallel}v_{\parallel} < 0$, reducing the resonance condition to

$$\omega(k_{\parallel}) + k_{\parallel}|v_{\parallel}| = \Omega_i. \quad (2)$$

To obtain the minimum wavenumber, $k_{\parallel} = k_c$, at which dissipation of the waves by cyclotron resonance with the background solar wind proton distribution occurs, we take $v_{\parallel} = v_{th,\parallel}$, where $v_{th,\parallel}$ is the parallel thermal speed of the proton velocity distribution, and for simplicity we substitute for $\omega(k_{\parallel})$ using the wave dispersion relation of Alfvén waves (e.g., Gary 1993): $\omega(k_{\parallel}) = k_{\parallel}v_A$,

$$k_c = \frac{\Omega_i}{v_A + v_{th,\parallel}} \equiv \frac{1}{d_i + \sigma_i}. \quad (3)$$

Here, σ_i is the pseudo-gyroscale, defined as $v_{th,\parallel}/\Omega_i$ using the parallel proton temperature, $T_{i,\parallel}$, which we distinguish from the typical definition of the ion gyroscale, ρ_i . The waves do not necessarily need to be parallel-propagating for resonance to occur; as long as there is a large enough k_{\parallel} component, a wave can resonate with the proton population, even if it also has a significant k_{\perp} component. If there is a substantial population of AICs in the solar wind, then we may expect the spectral break to occur at the scale $1/k_c$.

Several past studies have explored the physical processes behind the observed spectral steepening by comparing characteristic ion scales with the spectral break measured from in situ data (Leamon et al. 1998b, 2000; Smith et al. 2001; Markovskii et al. 2008; Perri et al. 2010; Bourouaine et al. 2012; Bruno & Trenchi 2014; Chen et al. 2014; Roberts et al. 2017; Wang et al. 2018) or through simulations (e.g., Ghosh et al. 1996; Howes et al. 2008b; Cerri et al. 2016; Franci et al. 2016, 2017). However, these studies have produced various different conclusions, and there is currently no consensus on the dominant dissipation mechanism. The difficulty in determining the break scale arises from the fact that the measured scales d_i and ρ_i at 1 au are linked by the proton perpendicular plasma beta, $\beta_{i,\perp} = n_i k_B T_{i,\perp}/(B_0^2/2\mu_0)$,

$$\frac{\rho_i}{d_i} = \sqrt{\beta_{i,\perp}}, \quad (4)$$

and typically $\beta_{i,\perp} \sim 1$, so that these scales are inseparable, except in cases where $\beta_{i,\perp} \ll 1$ or $\beta_{i,\perp} \gg 1$ (for example, see Chen et al. 2014). Therefore, the spectral break may be associated with different scales, depending on changing solar wind conditions.

1.2. Coherent Helicity Signature at High Frequencies

We can gain a better understanding of the possible dissipation mechanisms by looking at the nature of the fluctuations at these frequencies. The presence of fluctuations with different properties such as polarization will limit the role of certain mechanisms under different conditions. A useful quantity that can be used to diagnose certain types of fluctuations is the magnetic helicity, which characterizes the solenoidal structure of the magnetic field and twistedness of

field lines (Moffat 1978; Woltjer 1958, see also Smith 2003; Telloni et al. 2013). For solar wind turbulence, the quantity of interest is the fluctuating magnetic helicity density (Matthaeus & Goldstein 1982a). A reduced form, $H_m(k)$, can be computed from single-spacecraft measurements; based on several assumptions (Batchelor 1970; Montgomery & Turner 1981; Matthaeus et al. 1982), this is

$$H_m(k) = \frac{2 \operatorname{Im}\{\mathbf{P}_{yz}(k)\}}{k}, \quad (5)$$

where \mathbf{P}_{yz} is the y - z component of the reduced power spectral tensor of the magnetic field fluctuations in geocentric solar ecliptic (GSE) coordinates (for details on reduced spectra, see Wicks et al. 2012). We define the reduced normalized magnetic helicity, $\sigma_m(k)$, as

$$\sigma_m(k) = \frac{kH_m(k)}{E_b(k)} \equiv \frac{2 \operatorname{Im}\{\mathbf{P}_{yz}(k)\}}{\operatorname{Tr}\{\mathbf{P}_{ij}(k)\}}. \quad (6)$$

Here, $E_b(k)$ is the reduced magnetic spectral energy, which is given by the trace of the reduced power spectral tensor: $\operatorname{Tr}\{\mathbf{P}_{ij}\} = P_{xx} + P_{yy} + P_{zz}$. The normalized magnetic helicity gives a dimensionless measure of the polarization of magnetic fluctuations to identify wave modes at a particular frequency in the turbulent spectrum; σ_m is zero for linearly polarized waves and ± 1 for right- or left-hand circularly polarized fluctuations, respectively.

Past studies using a global mean magnetic field have found a lack of coherent helicity at low frequencies in the inertial range, i.e., fluctuating almost randomly between negative and positive values (Matthaeus & Goldstein 1982a). However, at ion-kinetic frequencies there is a dominant coherent signature that suggests right-hand polarization for outward propagating fluctuations (Goldstein et al. 1994; Leamon et al. 1998b; Hamilton et al. 2008; Brandenburg et al. 2011; Markovskii et al. 2015). More recently, wavelet-based studies (Telloni et al. 2012 and references therein) using the technique first developed by Horbury et al. (2008) for local mean field analysis have been employed (see also Podesta 2009; Wicks et al. 2010; Forman et al. 2011; Podesta & Gary 2011b, for more details). These studies attribute the right-handed signature to the presence of KAWs propagating at large angles to the local mean field and have also revealed the presence of a weaker left-hand polarized component likely due to quasi-(anti)parallel-propagating AICs (He et al. 2011, 2012a, 2012b; Podesta & Gary 2011b; Klein et al. 2014; Bruno & Telloni 2015; Telloni et al. 2015).

From these results, we may interpret the coherent helicity signature first observed by Goldstein et al. (1994) as arising from the dominance of the right-handed component over the left-handed component, implying dissipation of AICs at these frequencies that may be due to proton cyclotron resonance. In fact, Bruno & Telloni (2015) showed that on transitioning from fast to slow wind in the trailing edge of a fast wind stream (i.e., for decreasing Alfvénicity), both signatures weaken and eventually disappear, although the left-handed component is first to fade completely. However, Howes & Quataert (2010) showed that KAWs alone can also reproduce the observed helicity signature without the need for cyclotron resonance.

In this paper, we present a rigorous analysis of solar wind turbulence at ion-kinetic frequencies using a combined

identification of the frequency of the spectral break and onset of the magnetic helicity signature. We compare these spectral properties of the fluctuating magnetic field with the characteristic plasma scales, d_i , ρ_i , and $1/k_c$, and attempt to link the coherent helicity signature with the spectral steepening to help identify possible dissipation mechanisms at these frequencies. We use magnetic field spectra at a much higher resolution than undertaken previously so that plasma scales do not vary considerably over the time series of data used to compute the spectra. Our use of a large data set over the course of a year also enables us to identify how changing solar wind conditions affect possible dissipation mechanisms. We find evidence of proton cyclotron resonance that occurs at least half the time in our studied interval, particularly in the more Alfvénic fast wind, and discuss the possible implications for plasma heating at ion-kinetic scales.

2. Data Analysis and Results

For this study, we use data from the *Wind* spacecraft (Acuña et al. 1995), which launched in 1994. It moved permanently to the L1 point in 2004, providing almost 14 years of continuous in situ solar wind measurements. We obtain high-resolution 11 Hz (every 0.092 s) magnetic field measurements in GSE coordinates from the Magnetic Field Investigation (MFI) instrument (Lepping et al. 1995), using the calibration of Koval & Szabo (2013), and ion moments at a resolution of 92 s, including solar wind speed, v_{sw} , proton density, n_i , and proton temperatures, $T_{i,\parallel}$ and $T_{i,\perp}$, from the Solar Wind Experiment (SWE) instrument (Ogilvie et al. 1995), using the fitting technique described by Maruca & Kasper (2013). We preprocess the magnetic field data by removing small data gaps (<10 measurements, about 1 s of data) with linear interpolation, but leave larger gaps present. Similarly, we interpolate over small data gaps (<3 measurements, about 5 minutes) for the plasma moments. We also remove any plasma data from our analysis flagged as having unreliable fitting and remove manually any unphysical and anomalous measurements not identified by flagging. We use an entire year of data from 2012 in our analysis; this large data set outweighs the presence of a small number of large data gaps, while any smaller gaps that are interpolated should have a minimal impact on our overall results.

Due to the small amplitude of the turbulent fluctuations at ion-kinetic frequencies, instrumental and spacecraft-induced noise can lead to an artificial flattening of the power spectrum at the highest frequencies. For the MFI instrument, this “noise-floor” is thought to arise from the analog-to-digital conversion of the signal, the spacecraft spin, and spin-tone harmonics. The only past measurement for the noise level of the MFI instrument was by Lepping et al. (1995) (see Figure 3(b) therein), which was conducted on a prototype sensor before launch. To ensure that the amplitudes of power spectra at high frequencies are physical, we first determine the amplitude and frequency dependence of the MFI noise-floor from in-flight measurements before analyzing solar wind data. We provide details of this “noise-floor” determination in the Appendix and provide this data set for use in future studies.

2.1. Analysis of Solar Wind Spectra

To compute solar wind spectra, we employ a continuous wavelet transform (CWT) with a Morlet wavelet of

frequency-width $\omega_0 = 6$, using the method described by Torrence & Compo (1998). We obtain wavelet coefficients, $W(s,t)$, as functions of the scale, s , at which the wavelets are evaluated, and time. We then convert these scales into equivalent Fourier frequencies using $f \approx \omega_0/2\pi s$ and calculate components of the reduced power spectral tensor,

$$\mathbf{P}_{ij}(f,t) = W_i(f,t)W_j^*(f,t), \quad (7)$$

where the asterisk indicates complex conjugate and the indices describe the three GSE coordinates, $i, j = x, y, z$. The power spectral density (PSD) is then

$$\text{PSD}(f,t) = \frac{2}{f_s} \text{Tr}\{\mathbf{P}_{ij}(f,t)\}, \quad (8)$$

where $f_s = 10.87$ Hz is the sampling frequency of the MFI instrument. We first pad the signal to account for any border effects arising from the finite width of the Morlet wavelet, and then calculate an estimate of the PSD at each frequency for every measurement of the original time series. After removal of padding, we average the PSD over every 1000 MFI measurements. This averaging improves the accuracy of the amplitude of the power spectrum at each scale and results in one spectrum for every 92 s of data, which is the cadence of the SWE instrument. We take the time stamp of each 92 s spectrum as the middle of the time series used to produce that spectrum. Finally, we interpolate the time series of plasma measurements onto the time series of averaged PSD estimates to associate one measurement of the ion moments with each 92 s power spectrum.

We note that the length of time over which we average the spectra is shorter than the correlation time of solar wind turbulence, and so the assumptions of stationarity and ergodicity do not hold at low frequencies (Matthaeus & Goldstein 1982b; Perri & Balogh 2010). As such, many of the usual results of turbulence are not recovered; for example, the spectra do not converge to the typical $f^{-5/3}$ power law expected in the inertial range. However, we are attempting to measure turbulent behavior at ion-kinetic frequencies (0.1–5.4 Hz) and not in the inertial range. At these high frequencies there are a larger number of wavelengths sampled at these smaller scales during the advection of the turbulence past the spacecraft, and therefore the stationarity and ergodicity conditions are satisfied in our data set for our frequency range of interest.

2.2. Estimation of the Break Frequency

To estimate the break frequency of each spectrum, f_b , we fit the PSD to the following linear function:

$$\log_{10}(\text{PSD}) = m \log_{10}(f) + c, \quad (9)$$

where m is the gradient of the line or spectral exponent. To accommodate greater uncertainty in the spectra at low frequencies, we fit this function to the power spectra using windows in frequency that increase in width in logarithmic space toward lower frequencies, giving us a value for m for each window. The frequencies, f , for fitting Equation (9) to the spectrum included in each window are given by

$$\log_{10}(f_m) - 0.1j \leq \log_{10}(f) \leq \log_{10}(f_m), \quad (10)$$

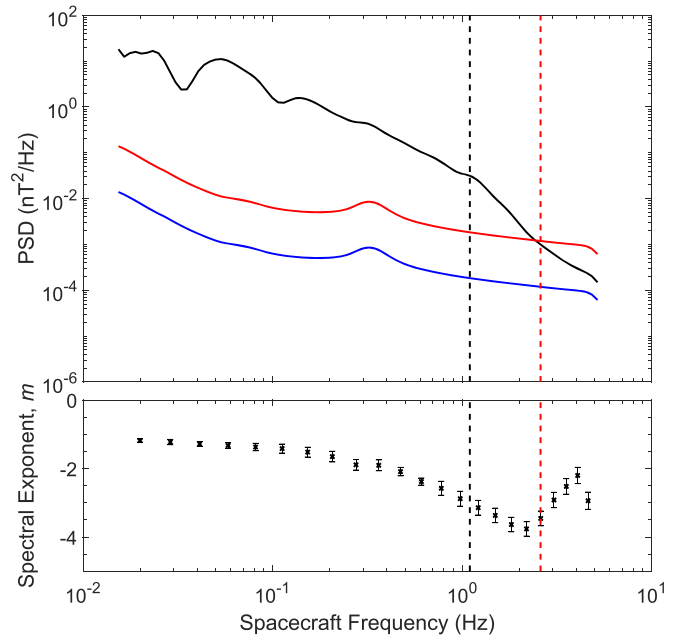


Figure 1. Top: an example 92 s power spectrum of the solar wind magnetic field, in black. The blue line is the MFI noise-floor from the Appendix, the red line is the noise-floor multiplied by a signal-to-noise ratio of 10, and the red dashed line is the noise cut-off frequency, f_{noise} (see main text). Bottom: results from the fitting of the function (Equation (9)) to the spectrum, showing the spectral exponent, m , for each window in our fitting process. Error bars show the root-mean-square error of the fitting. The black dashed line is our estimated break frequency, f_b .

where f_m is the maximum frequency within the window and the index, $j = 1, 2, 3, \dots$, increases by an integer factor for each successive window so that the term $0.1j$ widens the window as j increases. For each successive window, we set

$$\log_{10}(f_{m,j+1}) = \log_{10}(f_{m,j}) - 0.1j/20, \quad (11)$$

shifting the windows to lower frequencies as j increases. The division by 20 in the last term allows us to overlap the windows and provide a sufficient number of fits for m over the frequencies at which we evaluate the power spectra. We continue our windowing process along the spectrum as long as $\log_{10}(f_m) > -1$, giving us a total of 26 windows. The central frequency of each window, which we associate with a value of m , is taken as the median of the frequencies in that window.

We show an example 92 s spectrum from 2012 July in the top panel of Figure 1 and our results for m from our fitting process in the bottom panel. We see a change in m from about -1.2 to -3.8 from low to high frequencies, resulting from the transition between the power laws for the inertial range and the ion-kinetic range. This transition is not a simple step function because of the finite width of the fitting window at the frequency of the spectral break. To determine the width of this transition, we calculate two frequencies that bound either side of it. We identify the first, f_1 , when the difference between two successive values for m exceeds the threshold $|m_{j+1} - m_j| \geq 0.05$, and the second, f_2 , as the frequency with the minimum value for m . We then estimate the break frequency f_b for each spectrum as $f_b = (f_1 + f_2)/2$, in a similar fashion to Chen et al. (2014). The black dashed line in Figure 1 is our estimate of f_b for the example spectrum using this method, which we see agrees well with the break in the spectrum.

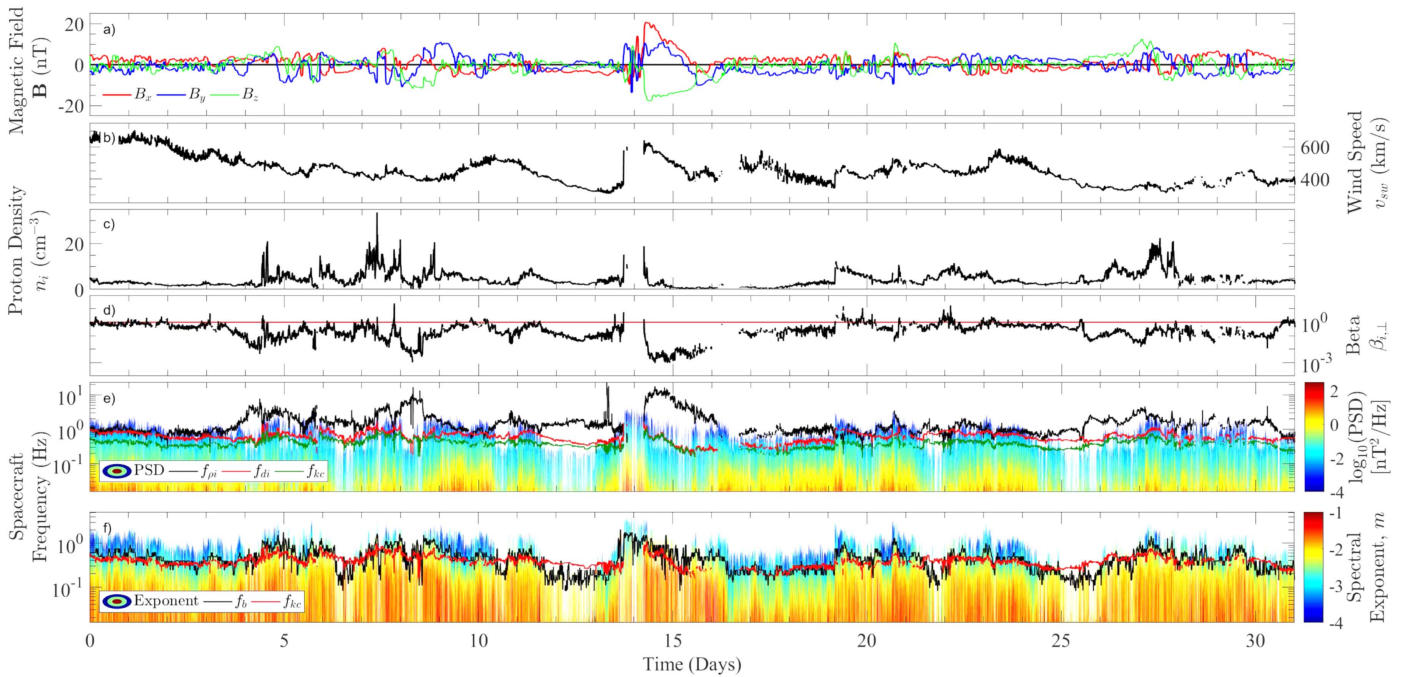


Figure 2. 2012 July time series of (a) the components of the magnetic field, \mathbf{B} , smoothed using a 51-point median filter, (b) the solar wind speed, v_{sw} , (c) the solar wind proton density, n_i , and (d) the proton perpendicular plasma beta, $\beta_{i,\perp}$. In panel (d), the red line indicates $\beta_{i,\perp} = 1$, where $\rho_i = d_i$ and therefore $1/k_c \approx \rho_i + d_i = 2\rho_i = 2d_i$, from Equations (3) and (4), assuming $\sigma_i \approx \rho_i$. (e) Contour plot of consecutive 92 s power spectra of the solar wind magnetic field. The white areas indicate large data gaps or data with frequencies $f \geq f_{noise}$. We show the characteristic plasma scales, $1/k_c$, d_i , and ρ_i , converted to frequencies using Taylor’s hypothesis (see main text) as the solid green, red, and black lines, respectively. (f) Contour plot of the spectral exponent, m , to the corresponding power spectra in panel (e). We also plot f_{kc} in red and the estimated f_b in black for comparison, which we smooth here by a 21-point median filter.

Toward higher frequencies in Figure 1, the spectrum flattens and m increases. This flattening is most likely due to the increasing contribution of instrumental noise to the signal at these frequencies. To ensure that our estimated f_b is physical, we determine a cut-off frequency, f_{noise} , where the spectrum is equal to a signal-to-noise ratio (S/N) of 10 times our noise-floor estimate (see the Appendix), indicated by the vertical red dashed line in Figure 1. We neglect an estimate of the break frequency if $f_b \geq f_{noise}$. Close to the Nyquist frequency, there is a second decrease in the spectral exponent, which we attribute to artifacts of the CWT.

To test the robustness of our automated fitting procedure and method to calculate f_b , we first apply it to consecutive 92 s power spectra over the course of one month, using data from 2012 July. Panels (a)–(d) in Figure 2 show time series of the components of the magnetic field, \mathbf{B} , the solar wind speed, v_{sw} , proton density, n_i , and proton perpendicular beta, $\beta_{i,\perp}$, respectively. We smooth \mathbf{B} using a 51-point median filter here to emphasize the sectoral structure of the interplanetary magnetic field from the numerous crossings of the heliospheric current sheet, highlighted by the changing sign of the B_x and B_y components. We see that v_{sw} varies between 300 and 700 km s^{-1} and n_i from less than 1 cm^{-3} to almost 35 cm^{-3} . There are several periods, often during fast wind intervals, where $\beta_{i,\perp} \sim 1$. At other times $\beta_{i,\perp}$ typically does not exceed unity and reaches a minimum value of almost 1×10^{-3} . The spacecraft sampled periods of both slow and fast wind, as well as shocks, density enhancements, and transient ejecta, illustrating the variability of the solar wind during this interval.

Panel (e) in Figure 2 shows a contour plot of consecutive 92 s power spectra over 2012 July, i.e., a time series of spectra over the course of a month. In comparison with panels (a)–(d), we see that the spectra and therefore, the turbulent processes in

the solar wind, depend on the overall plasma conditions, particularly at high frequencies. Here, white areas indicate data that we have removed, either due to the presence of a large data gap or because the frequencies exceed the defined noise-floor cut-off, f_{noise} . We also show as solid lines the three characteristic plasma scales, $1/k_c$, d_i , and ρ_i , in green, red, and black, respectively. We plot these three scales as frequencies assuming Taylor’s hypothesis: $f_L = v_{sw}/2\pi l$, where l is the appropriate length scale. According to panel (e), there are several periods during which $f_{noise} < f_L$, emphasizing the importance of our noise-floor treatment.

In Figure 2(f) we show a contour plot of the spectral exponent, m , versus frequency for each corresponding spectrum in panel (e), along with our estimated f_b and f_{kc} in black and red, respectively, for comparison. We note that the break frequencies are discretized by the scales of the wavelets and hence the windowing process in our fitting procedure. We discard values where $f_b \geq f_{noise}$, and also $f_b \leq 0.1 \text{ Hz}$. This second condition allows us to avoid times when the amplitude of fluctuations is so low that a physical break between two power laws is obscured by noise, and therefore an estimate for f_b by our automated method is unreliable. We smooth f_b here only for this figure using a 21-point median filter. We find that our fitting procedure performs an accurate estimate of f_b for the $\sim 29,000$ spectra from 2012 July, since f_b agrees well with the break in the spectrum from visual inspection of panel (f).

We now compare the three plasma scales as frequencies, f_L , with f_b , where $L = 1/k_c$, d_i , and ρ_i , and extend our analysis to a year of data from 2012. We calculate $\sim 344,000$ spectra, estimating f_b for each spectrum and comparing it to the corresponding values for the characteristic plasma scales, f_L . Figure 3 shows two-dimensional histograms for f_b with f_{kc} , f_{di} , and f_{ρ_i} in the top, middle, and bottom rows, respectively. We

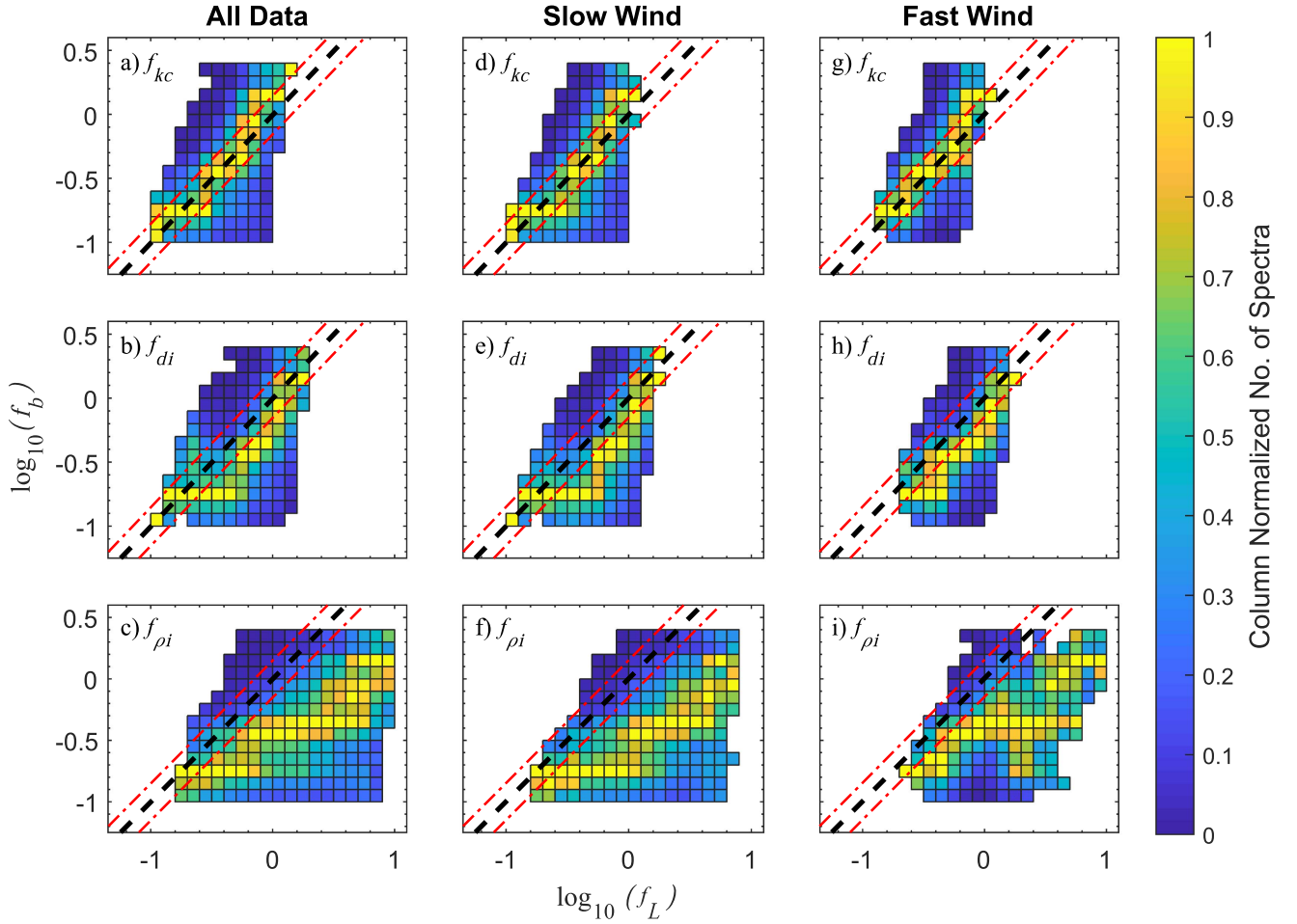


Figure 3. (a)–(c) Histograms for 2012 of the estimated break frequency, f_b , vs. the three characteristic plasma scales, converted into frequencies using Taylor’s hypothesis— f_L represents f_{kc} , f_{di} , and $f_{\rho i}$, for each row respectively. (d)–(f) The corresponding results for only slow wind ($<400 \text{ km s}^{-1}$) intervals. (g)–(i) The corresponding results for only fast wind ($>500 \text{ km s}^{-1}$) streams. The color bar represents the column-normalized number of spectra. The black dashed lines represent $f_b = f_L$, and similarly the red dashed lines are $f_b = f_L \sqrt{2}$ and $f_b = f_L / \sqrt{2}$, which give the resolution of the wavelet transform about the line $f_b = f_L$.

show the results for all data and then separate according to slow ($v_{\text{sw}} < 400 \text{ km s}^{-1}$) and fast wind ($v_{\text{sw}} > 500 \text{ km s}^{-1}$) in the left, middle, and right columns, respectively. Separating by wind speed allows us to test for systematic effects due to the large-scale structure of different solar wind streams. We normalize each column of the binned data in each plot by the maximum number of spectra in a bin for that column, highlighting the most probable f_b measured as a function of f_L . We neglect values for f_b when $f_b \geq f_{\text{noise}}$ and $f_b \leq 0.1 \text{ Hz}$, as discussed before. We also omit bins with ≤ 10 spectra to avoid undersampling. In each panel, the black dashed lines give the line $f_b = f_L$, and similarly the red dashed lines are $f_b = f_L \sqrt{2}$ and $f_b = f_L / \sqrt{2}$, which indicate the resolution of the wavelet transform about the line $f_b = f_L$ due to the finite width of the Morlet wavelet in frequency space (i.e., the e -folding frequency, see Torrence & Compo 1998).

To quantify the relationship between f_b and f_L , we conduct a statistical analysis using this year of data. We first calculate the Pearson correlation coefficient,

$$R(f_b, f_L) = \frac{1}{N-1} \sum_{i=1}^N \left(\frac{f_{b,i} - \mu_b}{\sigma_b} \right) \left(\frac{f_{L,i} - \mu_L}{\sigma_L} \right), \quad (12)$$

where μ is the mean and σ is the standard deviation. The coefficient $R \in [-1, +1]$ measures the linear correlation between f_b and f_L . A value of $R = \pm 1$ indicates a positive or negative linear correlation, respectively, whereas zero indicates no linear correlation. If $|R| = 1$, a linear equation describes the relationship between the variables f_b and f_L . We also define a residual, ρ , which in analogy to the standard deviation is

$$\rho(f_b, f_L) = \sqrt{\frac{1}{N-1} \sum_{i=1}^N |f_{b,i} - f_{L,i}|^2}, \quad (13)$$

where $\rho \geq 0$. The residual gives the difference between our measured f_L and estimated f_b ; in other words, a value of ρ closer to zero indicates there is less spread of data about the line $f_b = f_L$. In our calculations of R and ρ , we take the logarithms of both f_b and f_L . We place more weight here on the statistical significance of ρ over R since a linear relationship does not necessarily imply that $f_b = f_L$. The correlation coefficients are also intrinsically linked because of the definition of $1/k_c$ and the fact that ρ_i and d_i differ only by a factor of $\sqrt{\beta_{i,\perp}}$. As a final test, we count the number of spectra that lie between the two red dashed lines in each panel of Figure 3 to determine a

Table 1Correlation Coefficients, Residuals, and Percentages for f_L and f_b from the Data Shown in Figures 3 and 4

	Plasma Scale L	Correlation R	Residual ρ	Percentage (%)
All Data	$1/k_c$	0.56	0.17	52.08
	d_i	0.52	0.25	30.19
	ρ_i	0.34	0.43	9.14
Slow	$1/k_c$	0.54	0.12	49.42
	d_i	0.48	0.19	27.74
	ρ_i	0.38	0.33	6.41
Fast	$1/k_c$	0.58	0.06	57.01
	d_i	0.58	0.08	36.08
	ρ_i	0.32	0.14	15.66
$\beta_{i,\perp} \sim 1$	$1/k_c$	0.60	0.02	51.81
	d_i	0.61	0.04	26.44
	ρ_i	0.61	0.04	26.42

percentage of the total number of spectra that satisfy $f_b \simeq f_L$, within the e -folding frequency. For the total number of spectra, we do not include instances where there are large data gaps, and where we have discarded values for f_b . For instances where we filter data according to slow or fast wind, the total number of spectra we use is only for that filtered data set. We give the results of our statistical analysis in Table 1.

For all 2012 data, regardless of wind speed, both f_{kc} and f_{di} have moderate correlations with f_b , with values of $R = 0.56$ and $R = 0.52$, respectively, whereas the correlation for f_{ρ_i} is weaker at $R = 0.34$. The lowest residual is $\rho = 0.17$ for f_{kc} , while for f_{di} it is $\rho = 0.25$ and for f_{ρ_i} it is even higher at $\rho = 0.43$. These values show that the cyclotron resonance scale, $1/k_c$, is most closely associated with the spectral break (i.e., closest to $f_b \simeq f_L$) during the interval we study. This finding is supported by 52.08% of the total number of spectra in our data set falling between the two red dashed lines for f_{kc} in Figure 3(a). In contrast, we find only 30.19% for f_{di} in panel (b) and 9.14% for f_{ρ_i} in panel (c). The gyroscale, ρ_i , therefore has a poor relationship with the break frequency, suggesting that it is overall least likely to be associated with the spectral steepening during the interval we study.

These findings hold when we separate the data according to wind speed. For slow wind, f_{kc} has the highest correlation coefficient at $R = 0.54$ and lowest residual at $\rho = 0.12$. During periods of fast wind streams, the residual for f_{kc} is about half that of slow wind at $\rho = 0.06$, the smallest for all three scales. From panels (d) and (g) in Figure 3, we are unable to visually differentiate between the cases of fast and slow wind without statistical analysis. Also, comparing panels (f) and (g), we find that 57.01% of spectra fall within the resolution limit of our wavelet transform for f_{kc} in fast wind, which is higher than the 49.42% for slow wind. The correlation coefficients for both f_{kc} and f_{di} in fast wind are equal, at $R = 0.58$, which is only slightly larger than their slow wind values. Transitioning from slow to fast wind in panels (e) and (h), the percentage of spectra where $f_b \simeq f_{di}$ increases from 27.74% to 36.08%. From these values, we see that the relationship between f_{kc} and f_b is better than for f_{di} and maintained even when the large-scale stream structure of the wind varies, although it is strongest in fast wind streams.

According to Equations (3) and (4), $1/k_c$ will coincide with the larger of the two scales, d_i or ρ_i , when $\beta_{i,\perp} \ll 1$ or $\beta_{i,\perp} \gg 1$, respectively, assuming an isotropic temperature (i.e., $\rho_i \simeq \sigma_i$). This expectation is consistent with observations by Chen et al. (2014) showing that the spectral break occurs at d_i for $\beta_{i,\perp} \ll 1$ and at ρ_i for $\beta_{i,\perp} \gg 1$, which they note is consistent with a break at $1/k_c$ in both cases. However, by definition, when $\beta_{i,\perp} \sim 1$, $\rho_i \simeq d_i$ and therefore $1/k_c \simeq \rho_i + d_i \simeq 2\rho_i \simeq 2d_i$. Indeed, for periods with $\beta_{i,\perp} \sim 1$ we see in Figures 2(d)–(f) that f_{di} and f_{ρ_i} coincide and f_{kc} is shifted to lower frequencies by about a factor of 2. During these periods, there is a good agreement between f_{kc} and f_b . To address what happens when $\beta_{i,\perp} \sim 1$ quantitatively and clearly show the difference between $1/k_c$ and d_i or ρ_i , we filter our year of data to include only periods where $0.95 \leq \beta_{i,\perp} \leq 1.05$ and show the corresponding 2D histograms in Figure 4. In addition, the results from our statistical analysis are shown in the bottom panel of Table 1. We note that we do not remove bins with ≤ 10 spectra here because of the smaller amount of data available for these periods, but this only affects bins furthest from the black dashed line.

Comparing panels (b) and (c) to (a) in Figure 4, we see that our measured f_b is consistently shifted to frequencies lower than f_{di} and f_{ρ_i} , i.e., the yellow enhancement in panels (b) and (c) is below the black dashed line, but in panel (a) we see that it is closer to the dashed line. These plots show that $1/k_c$ is a more likely candidate for the break scale than d_i or ρ_i , and we quantify this result by calculating R and ρ for this data set. The correlation coefficients are the same for f_{di} and f_{ρ_i} at $R = 0.61$, and almost the same at $R = 0.60$ for f_{kc} ; however, the latter has the lowest residual at $\rho = 0.02$, compared to $\rho = 0.04$ for f_{di} and f_{ρ_i} . We note that the statistics for f_{ρ_i} improve considerably when considering only periods of $\beta_{i,\perp} \sim 1$, and are the same in this case for f_{di} . Again, we find a high percentage of the number of spectra where $f_b \simeq f_{kc}$ at 51.81%, almost double that for the other two scales.

When we consider all data in our interval, the results from our statistical analysis for f_{kc} and f_{di} do not differ significantly, particularly in fast wind, as we see from similar values for R and ρ in Table 1. From our analysis of periods where $\beta_{i,\perp} \sim 1$, we explain this result as being due to the ratio of spectra where $\beta_{i,\perp} < 1$ to those where $\beta_{i,\perp} > 1$, which is almost 8 in our data set. Finally, we conclude that f_b is best associated with f_{kc} and so the spectral break is most likely related to proton cyclotron resonance. We then explain the correlations with d_i and ρ_i as being due to the dependence of $1/k_c$ on both variables, and the fact that d_i and ρ_i are separated only by a factor of $\sqrt{\beta_{i,\perp}}$.

2.3. Quantification of the Helicity Signature

To further explore the possible role of proton cyclotron resonance at ion-kinetic frequencies, we now investigate the nature of the fluctuations at these frequencies. We calculate helicity spectra from successive periods of 92 s using the normalized magnetic helicity, σ_m , from Equation (6). Again, we use Taylor's hypothesis to obtain σ_m as a function of frequency instead of wavenumber, giving us one helicity spectrum for each corresponding power spectrum from the previous section. To quantify the relationship between $1/k_c$ and the coherent helicity signature at high frequencies, we devise a method to calculate the onset frequency, f_h , of the helicity signature, defined as the threshold frequency at which we see an enhancement in the helicity at ion-kinetic scales. We first fit

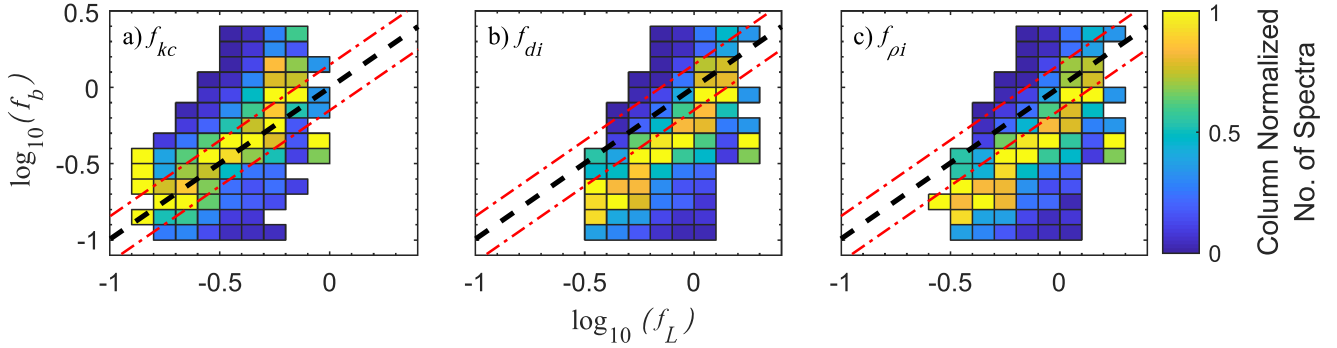


Figure 4. Histograms for 2012 of the estimated break frequency, f_b , vs. the three characteristic plasma scales, converted into frequencies using Taylor’s hypothesis— f_L represents f_{kc} , f_{di} , and f_{pi} for each panels (a), (b), and (c) respectively. The data used are for periods where $0.95 \leq \beta_{i,\perp} \leq 1.05$. The color bar represents the column-normalized number of spectra. The black dashed lines represent $f_b = f_L$, and similarly the red dashed lines are $f_b = f_L\sqrt{2}$ and $f_b = f_L/\sqrt{2}$, which give the resolution of the wavelet transform about the line $f_b = f_L$.

a Gaussian function to the helicity spectra,

$$\sigma_m = \frac{1}{\sqrt{2\pi}\sigma_D} \exp\left\{-\frac{(f-f_p)^2}{2\sigma_D^2}\right\}, \quad (14)$$

where the fitting parameters are the standard deviation, σ_D , and the mean, f_p , which corresponds to the frequency of the peak in the helicity signature. We perform the Gaussian fitting in linear space so that the method is biased toward the peak in helicity at the highest frequencies, i.e., the coherent helicity signature. We show in the top panel of Figure 5 the example power spectrum from Figure 1, along with its corresponding helicity spectrum in the bottom panel, both in black. In the bottom panel, we also plot in red the Gaussian fit to the helicity spectrum using Equation (14). The red dashed line gives f_p from the fitting, whereas the black and gray dashed lines are f_b and f_{noise} from before, respectively. To estimate the onset frequency f_h , we calculate the FWHM of the Gaussian peak using $\Delta f = \sigma_D\sqrt{8\ln(2)}$ and then

$$f_h = f_p - \Delta f/2. \quad (15)$$

The minus sign is used to determine the onset frequency bounded toward lower frequencies. This method is independent of whether the peak in helicity is negative or positive and allows for an automated process estimating both f_h and f_p for $\sim 344,000$ helicity spectra. In Figure 5, f_h is given by the blue dashed line. We see that f_b and f_h are separated by only about 0.1 Hz. From the results of Section 2.2, this result implies that f_h may also be associated with f_{kc} and suggests that the presence of the helicity signature is related to cyclotron resonance. We further investigate this relationship between f_b and f_h using our statistical analysis from the previous section. We also follow up the work of Markovskii et al. (2015) to confirm a relationship between f_p and f_{pi} using our data set.

We first use our method described above to estimate both f_h and f_p for 2012 July in order to check that it accurately reproduces the features of the helicity spectra. In Figures 6(a) and (b) we show again time series of \mathbf{B} and v_{sw} for 2012 July. In addition, panels (c) and (d) show contour plots of σ_m for consecutive 92 s spectra over the course of 2012 July, where we normalize the frequency of each spectrum by $1/f_{kc}$ in panel (c), and similarly by $1/f_{pi}$ in panel (d). We also plot the

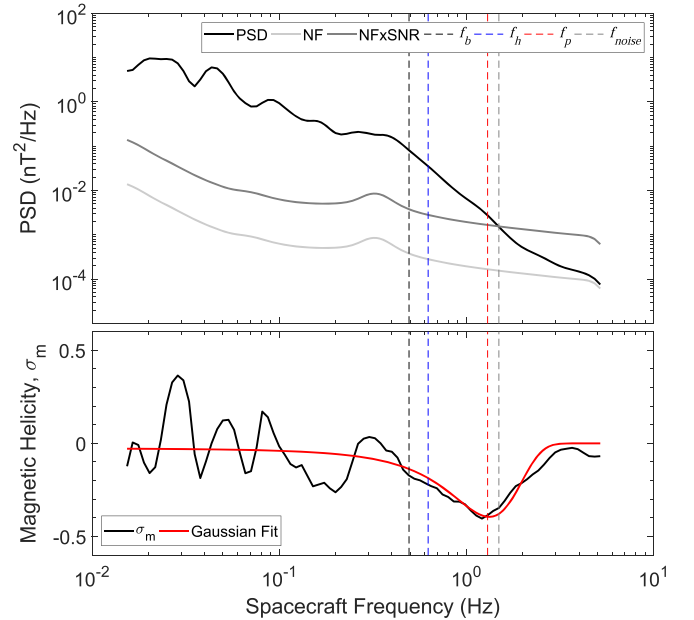


Figure 5. Top: an example 92 s power spectrum of the solar wind magnetic field from Figure 1, in black. The light gray line is the MFI noise-floor from the Appendix, the dark gray line is the noise-floor multiplied by a signal-to-noise ratio of 10, and the gray dashed line is the noise cut-off frequency, f_{noise} (see main text). The black dashed line is our estimated break frequency, f_b , from before. Bottom: the corresponding 92 s magnetic helicity spectrum, σ_m , in black and the fitting of the Gaussian function (Equation (14)) to the spectrum in red. The coherent helicity signature at high frequencies is well represented by the Gaussian peak. From our fitting, we obtain the helicity onset frequency, f_h , from Equation (15) and the peak helicity frequency, f_p , from the mean of the Gaussian peak, given by the blue and red dashed lines, respectively.

lines $f_{kc} = 1$ and $f_{pi} = 1$ for reference in red, as well as our estimated f_h and f_p in black, in panels (c) and (d), respectively. We normalize the spectra here only for the figure, and not in any future analysis. From panel (c), we can see that f_h bounds at lower frequencies the enhanced red and blue signature as we expect. Also, from panel (d) we see that the peak of the helicity signature is located close to the middle of the helicity signature before the enhancement disappears completely (it should not be located directly in the middle due to the logarithmic scale in frequency). Therefore, we conclude that our method works and quantifies the onset and peak of the helicity signature accurately. We will now discuss our findings from Figure 6 in more detail.

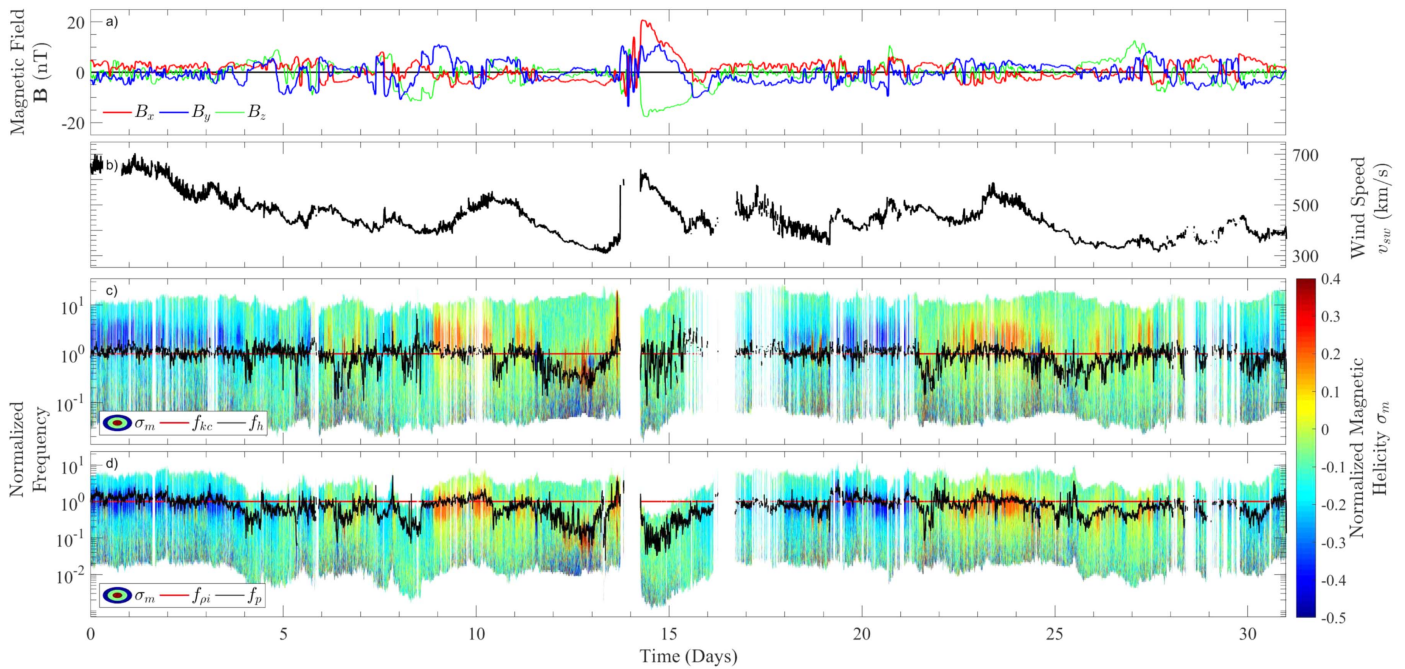


Figure 6. 2012 July time series of (a) the components of the magnetic field, \mathbf{B} , smoothed using a 51-point median filter to highlight the sectoral structure of the solar wind, and (b) the solar wind speed, v_{sw} , repeated from Figure 2. (c) Contour plot of consecutive 92 s reduced normalized magnetic helicity, σ_m , spectra from 2012 July, corresponding to each power spectrum in Figure 2(e). The spectra have been normalized by $1/f_{kc}$, and we plot the line $f_{kc} = 1$ in red for reference. We also show the estimated helicity onset frequency, f_h , in black. (d) Similar to panel (c), where the spectra are normalized instead by $1/f_{pi}$, and we plot the line $f_{pi} = 1$ in red for reference. We also show the estimated helicity peak frequency, f_p , in black. Both f_h and f_p are smoothed here by a 21-point median filter.

The persistent band of enhancement in σ_m at higher frequencies varies between about -0.4 and $+0.2$. Figure 6(a) suggests that the sectoral structure of the solar wind is likely responsible for this changing sign in helicity over the course of the month, which is consistent also with the findings of He et al. (2011). From Figure 6(c), we can see that the positive helicity signal is typically weaker in amplitude than the negative signal by a factor of 2. We currently have no explanation for this finding, but it is an interesting observation that should be explored in another study. We see that when an enhancement in helicity signature is present at high frequencies, f_h is well correlated with f_{kc} . By comparing panels (b) and (c), we find that the helicity enhancement weakens or almost completely disappears during periods of slow solar wind. Both these results show that the findings of Bruno & Telloni (2015) and Telloni et al. (2015) apply to large volumes of the solar wind. Also, from Figure 6(d), the peak of this coherent helicity signature is correlated with f_{pi} , especially in fast wind where the helicity signature is strongest, which is consistent with Markovskii et al. (2015) and Telloni et al. (2015). While we have not shown a similar plot for $f_{di} = 1$, we find that it is not closely associated with either f_h or f_p , and confirm this in our subsequent analysis.

At lower frequencies than f_{kc} , the helicity fluctuates about zero, as expected for the inertial range of solar wind turbulence (Matthaeus & Goldstein 1982a), showing either a lack of or no dominant coherent circular polarization of fluctuations. There is an enhanced signature in the helicity that significantly deviates from the characteristic plasma scales between July 12 and July 16, peaking at around 0.1 Hz (from Figure 6(c), about 0.5 in normalized frequency units). We associate this signature with AICs produced by instabilities from unstable particle distributions. These waves are often Doppler-shifted toward lower frequencies than the spectral break since they typically

propagate toward the Sun, in the opposite direction to the turbulent magnetic fluctuations we consider here (e.g., see Tsurutani et al. 1994; Jian et al. 2009, 2010, 2014; Gary 2015; Roberts & Li 2015; Roberts et al. 2015; Wicks et al. 2016). To exclude these events from our analysis, we discard data with $f_h \leq 0.2$ Hz and $f_p \leq 0.2$ Hz.

At frequencies $f > f_p$, the enhancement disappears, and the helicity returns to a value close to zero. If the trace of the power spectral tensor is increased artificially by instrumental noise, then the helicity will also reduce to zero, by definition from Equation (6). In fact, the increasing contribution from noise should not affect the phase contribution to the helicity, but rather just its amplitude. Therefore, despite seeing a return to zero, we do not see the return of the signature to an incoherent one similar to that at low frequencies seen in Figure 6, where σ_m oscillates in color between red and blue for opposite polarizations. Instead, the signal remains coherent with a value close to zero for $f > f_p$. Therefore, we cannot determine whether this effect is physical or due to the MFI noise-floor. An alternative explanation is aliasing (see the Appendix). Despite this, we find that typically $f_p < f_{noise}$ and therefore we take the peak in the helicity signature, and hence f_p , as physical.

We now extend our analysis to include an entire year of data from 2012 in the same way as in Section 2.2. In Figure 7 we show histograms in the same format as Figure 3 for f_L against f_h for all data and then separated into periods of slow and fast wind in panels (a)–(c), (d)–(f), and (g)–(i), respectively. In Figure 8 we show, in a similar fashion to Figure 4, f_L against f_h for periods where $\beta_{i,\perp} \sim 1$. Finally, in Figure 9 we plot histograms for f_L against f_p . Here, we discard data with $f_h \geq f_{noise}$ and $f_p \geq f_{noise}$ to ensure that instrumental noise does not affect our results, and data where $f_h \leq 0.2$ and $f_p \leq 0.2$ Hz, as discussed previously. We provide the results from our

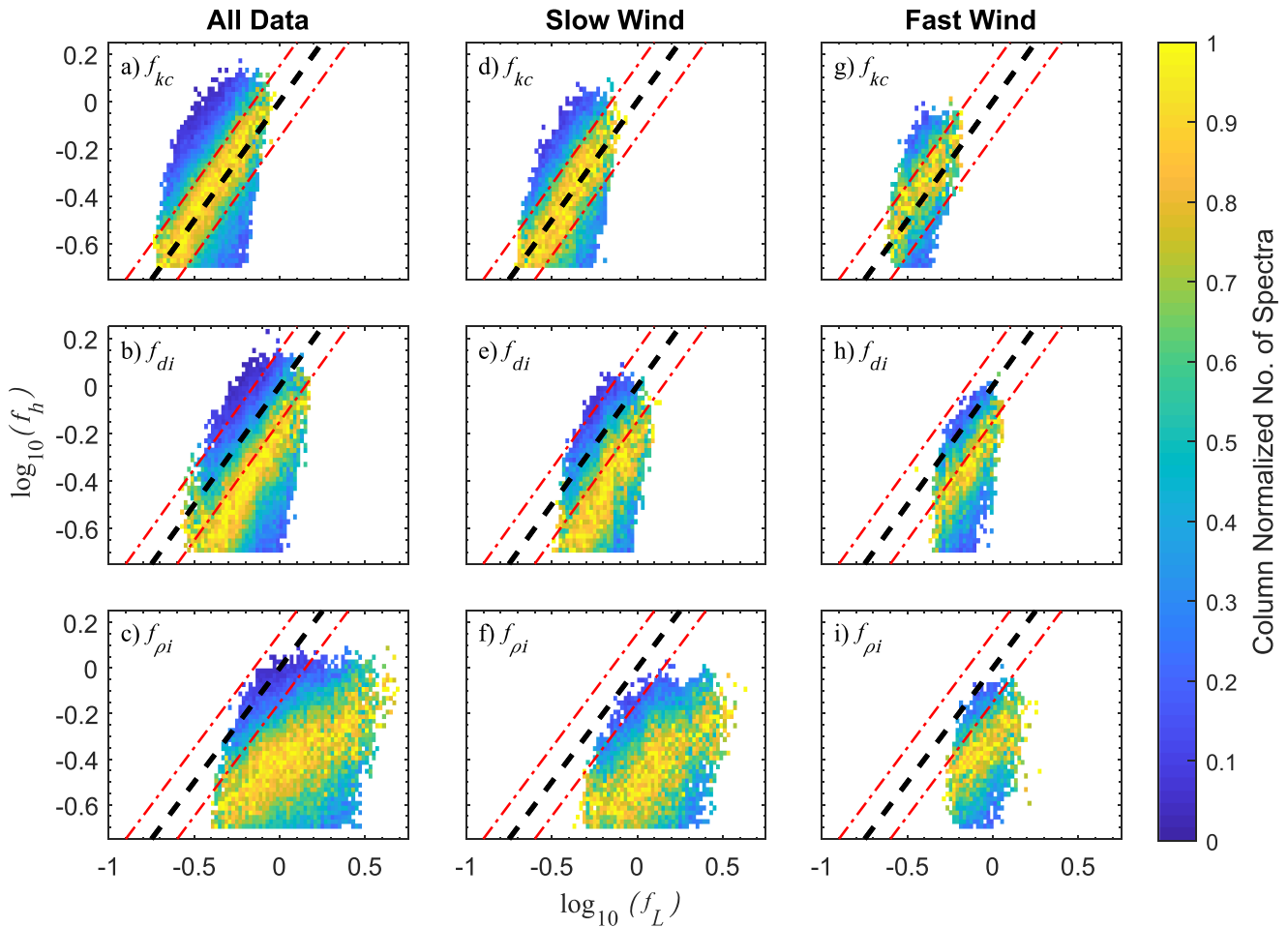


Figure 7. (a)–(c) Histograms for 2012 of the estimated helicity onset frequency, f_h , vs. the three characteristic plasma scales, converted into frequencies using Taylor’s hypothesis— f_L represents f_{kc} , f_{di} , and f_{pi} , for each row respectively. (d)–(f) The corresponding results for only slow wind ($<400 \text{ km s}^{-1}$) periods. (g)–(i) The corresponding results for only fast wind ($>500 \text{ km s}^{-1}$) streams. The color bar represents the column-normalized number of spectra. The black dashed lines represent $f_h = f_L$, and similarly the red dashed lines are $f_h = f_L \sqrt{2}$ and $f_h = f_L / \sqrt{2}$, which give the resolution of the wavelet transform about the line $f_h = f_L$.

statistical analysis for f_L and f_h in Table 2 and for f_L and f_p in Table 3.

We find that f_{pi} has the lowest correlations and highest residuals with f_h regardless of wind speed, which is consistent with Figure 7, where the distribution of data deviates significantly from the black dashed line. We conclude that f_{pi} is not directly comparable to f_h within our studied interval. When we consider all data, f_{kc} has the highest correlation coefficient of $R = 0.48$ and lowest residual of $\rho = 0.09$, compared to $R = 0.40$ and $\rho = 0.15$ for f_{di} . We find that 64.29% of the total number of spectra fall between the two red dashed lines for f_{kc} in Figure 7(a), compared to 33.37% for f_{di} in panel (b). These percentages are similar regardless of wind speed. Besides comparable correlation coefficients of about $R = 0.42$ – 0.45 in fast wind streams, f_{kc} is closer to the relationship $f_L \simeq f_h$ than f_{di} , from visual comparison of panels (g) and (h). In particular, we see that f_{kc} has the lowest residual of $\rho = 0.04$ during fast wind streams, compared to $\rho = 0.06$ in slow wind. Comparing panels (d) and (g), the percentage of spectra between the red dashed lines for f_{kc} is lower in the fast wind at 61.38% than in the slow wind where it is 64.72%, despite a lower residual in the former.

As in the previous section, we also filter the data to include only periods where $0.95 \leq \beta_{i,\perp} \leq 1.05$ and show the corresponding 2D histograms in Figure 8, as well as the results from

Table 2
Correlation Coefficients, Residuals, and Percentages for f_L and f_h from the Data Shown in Figures 7 and 8

	Plasma Scale L	Correlation R	Residual ρ	Percentage (%)
All Data	$1/k_c$	0.48	0.09	64.29
	d_i	0.40	0.15	33.37
	ρ_i	0.35	0.29	7.61
Slow	$1/k_c$	0.48	0.06	64.72
	d_i	0.39	0.10	32.71
	ρ_i	0.38	0.21	4.97
Fast	$1/k_c$	0.45	0.04	61.38
	d_i	0.42	0.06	35.33
	ρ_i	0.33	0.10	14.21
$\beta_{i,\perp} \sim 1$	$1/k_c$	0.46	0.01	62.29
	d_i	0.47	0.03	23.45
	ρ_i	0.47	0.03	23.32

our statistical analysis in the bottom panel of Table 2. Our results are similar to those for f_b and f_L , where we see clearly that f_{kc} best corresponds to f_h . From our statistical analysis, the correlation coefficients are the same for both f_{di} and f_{pi} at

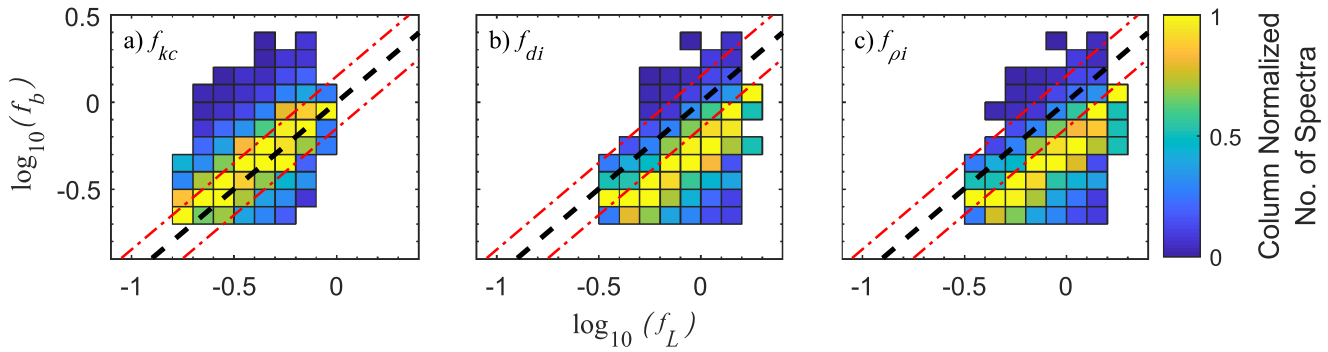


Figure 8. Histograms for 2012 of the estimated helicity onset frequency, f_h , vs. the three characteristic plasma scales, converted into frequencies using Taylor’s hypothesis— f_L represents f_{kc} , f_{di} , and $f_{\rho i}$, for panels (a), (b), and (c) respectively. The data used are for periods where $0.95 \leq \beta_{i,\perp} \leq 1.05$. The color bar represents the column-normalized number of spectra. The black dashed lines represent $f_h = f_L$, and similarly the red dashed lines are $f_h = f_L\sqrt{2}$ and $f_b = f_L/\sqrt{2}$, which give the resolution of the wavelet transform about the line $f_h = f_L$ due to the finite width of the Morlet wavelet in frequency space.

Table 3

Correlation Coefficients, Residuals, and Percentages for f_L and f_p from the Data Shown in Figure 9

	Plasma Scale	Correlation	Residual	Percentage
	L	R	ρ	(%)
All Data	$1/k_c$	0.55	0.19	16.83
	d_i	0.51	0.12	44.79
	ρ_i	0.34	0.15	46.62
Slow	$1/k_c$	0.56	0.11	19.52
	d_i	0.49	0.07	46.00
	ρ_i	0.41	0.11	39.82
Fast	$1/k_c$	0.52	0.08	14.15
	d_i	0.53	0.05	41.86
	ρ_i	0.28	0.06	51.74

$R = 0.47$, and almost the same at $R = 0.46$ for f_{kc} ; however, the latter again has the lowest residual at $\rho = 0.01$, compared to $\rho = 0.03$ for the other two scales. Again, we find a high percentage of the number of spectra where $f_b \simeq f_{kc}$ at 62.29%, almost triple that of the other two scales.

Following Section 2.2, we conclude that the onset of the helicity signature is also related to the cyclotron resonant scale, and therefore both the spectral steepening and coherent helicity signature are likely linked to the same physical process: proton cyclotron resonance. This signature is most prevalent when the spacecraft measures fast wind streams, and therefore we conclude that there is a stronger relationship between f_{kc} and f_h during these periods, as we also see for f_{kc} and f_b . The lower percentage for f_{kc} in fast wind is likely due to the smaller number of measurements available than for slow wind periods, as we see in plots in the right column of Figure 7, or because of the limited applicability of wind speed as the only criterion to categorize wind streams.

Moving now to the peak frequency of the helicity signature and our results presented in Figure 9 and Table 3, we find that f_{kc} and f_{di} have similar correlation coefficients with f_p of $R = 0.49$ – 0.56 , regardless of wind speed. We can also see little difference when comparing visually the three columns in the figure for these two scales. However, the lowest residuals are seen for f_{di} , giving $\rho = 0.07$ and $\rho = 0.05$ during slow and fast wind streams, respectively. We find that $f_{\rho i}$ has lower correlation coefficients at $R = 0.28$ – 0.41 than f_{kc} and f_{di} . However, its residuals are comparable to that of f_{di} , at $\rho = 0.06$

for fast wind and $\rho = 0.11$ for slow wind. Figure 9 shows that f_p correlates with both f_{di} and $f_{\rho i}$, as expected since they differ only by a factor of $\sqrt{\beta_{i,\perp}}$, but there is a constant offset in frequency for f_{di} that is not present for $f_{\rho i}$. When we consider all data, 46.62% of spectra satisfy $f_p \simeq f_{\rho i}$ compared to 44.79% for $f_p \simeq f_{di}$, within the e -folding frequency.

For frequencies $f_{\rho i} > 1$ Hz, the most likely value for f_p diverges from the black dashed line in panel (c) of Figure 9, which results in the low values for R with $f_{\rho i}$, and higher correlation with f_{di} . However, we find that 39.82% of spectra in slow wind and 51.74% in fast wind satisfy $f_p \simeq f_{\rho i}$ within the e -folding frequency. The higher percentage in fast wind is likely due to the presence of a stronger helicity signature than for slow wind, making detection easier. The divergence at high frequencies may be caused by undersampling, because f_p can exceed f_{noise} at these frequencies, but we try to account for this by discarding bins with ≤ 10 spectra. We also see a similar feature in panel (i) of Figure 7 as in panel (i) in Figure 3. Due to the noise-floor, it is difficult to distinguish whether this feature is physical or an artifact. Despite this divergence at high frequencies, we conclude that ρ_i better corresponds with the peak in the helicity signature at ion-kinetic frequencies than the other two scales.

3. Discussion

Our main result is the correlation of the cyclotron resonance scale, $1/k_c$, with the onset of a steepening in the power spectrum of magnetic field fluctuations and a coherent magnetic helicity signature at ion-kinetic scales. The helicity also reaches a maximum at scales comparable to ρ_i . Therefore, we suggest that these two signatures are related and result from proton cyclotron damping of AICs, leading to a steeper power law due to dissipation at these scales. We then explain the resulting helicity signature as being due to the residual population of KAWs left behind after the AICs are removed from the turbulent cascade. This cyclotron resonant dissipation is consistent with the shape of proton distributions observed in the fast wind (e.g., Marsch & Tu 2001; Tu & Marsch 2001, 2002; Marsch et al. 2004; Heuer & Marsch 2007; He et al. 2015a, 2015b). These results hold over most solar wind conditions, but in particular during periods of fast wind streams where the helicity signature is strongest.

We find that over the course of 2012, the onset of the coherent helicity signature corresponds to $1/k_c$ for 64.29% of the time, within the limits of the e -folding frequency of our

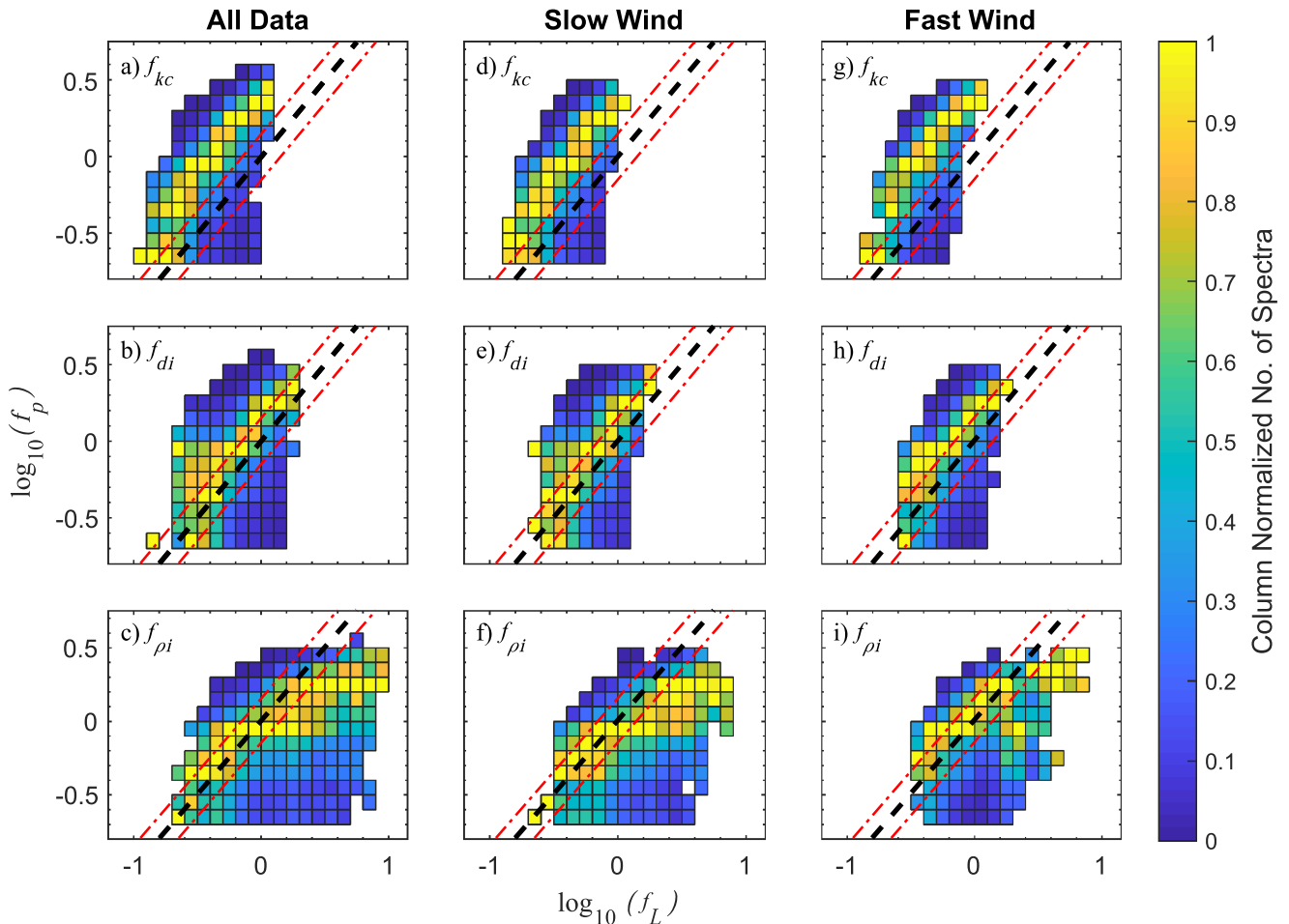


Figure 9. (a)–(c) Histograms for 2012 of the estimated helicity peak frequency, f_p , vs. the three characteristic plasma scales, converted into frequencies using Taylor’s hypothesis— f_L represents f_{kc} , f_{di} , and $f_{\rho i}$, for each row respectively. (d)–(f) The corresponding results for only slow wind ($<400 \text{ km s}^{-1}$) periods. (g)–(i) The corresponding results for only fast wind ($>500 \text{ km s}^{-1}$) streams. The color bar represents the column-normalized number of spectra. The black dashed lines represent $f_p = f_L$, and similarly the red dashed lines are $f_p = f_L \sqrt{2}$ and $f_p = f_L / \sqrt{2}$, which give the resolution of the wavelet transform about the line $f_p = f_L$.

Morlet wavelet. This value does not change significantly when we filter data according to wind speed. Given how we measure f_h using a Gaussian function, there is no reason for both f_h and f_{kc} to correlate well by random chance. The onset of the helicity peak determined from the FWHM does not necessarily need to occur at $1/k_c$, and yet we find they are closely related. Similarly, we find that 52.08% of the time the break scale corresponds to $1/k_c$. These results imply that cyclotron resonance with protons likely occurs at least half the time in the solar wind at ion-kinetic scales. However, the lower percentage for $f_b \simeq f_{kc}$ indicates that resonance with AICs may not always lead to a sufficient amount of energy being removed from the cascade to result in a spectral steepening at $1/k_c$. Alternatively, this may be due to the higher level of uncertainty in measuring the break scale than in measuring the onset of the helicity signature. We can also interpret the value of the square of the correlation coefficient, R^2 , as the percentage of the time that one parameter depends on another. From our results, this would give somewhat lower percentages (23%–31%) than our first estimates. We do not place too much weight on these correlation coefficients since they can be misleading, especially when considering our results for periods where $\beta_{i,\perp} \sim 1$. Therefore, we take our first calculation as a more reliable estimate.

The better agreement found in fast wind between $1/k_c$, the break scale, and the onset of the helicity signature suggests that cyclotron damping primarily occurs in fast wind streams, which are typically more Alfvénic with a higher population of AICs (Roberts & Li 2015; Lion et al. 2016; Telloni & Bruno 2016). However, we find that the coherent helicity signature disappears or significantly weakens during slow wind periods, in agreement with Bruno & Telloni (2015). The dispersion relation for Alfvén waves splits into KAWs or AICs at a critical angle to the magnetic field that is dependent on β_i (Gary 1986). Therefore, an explanation for the reduction in the prevalence of helicity signatures in the slow wind may be that different β_i in fast and slow wind streams affects how we observe the helicity signature. Despite the lack of a coherent helicity signature in the slow wind, we still observe a spectral steepening at $1/k_c$, but the agreement is weaker than in the fast wind.

The anisotropic nature of plasma turbulence in the solar wind implies a limited role of k_{\parallel} in the energy cascade in the inertial range, due to a higher amount of power in perpendicular wavenumbers (Horbury et al. 2008; Chen et al. 2010a, 2010b; Wicks et al. 2010). Despite this, we find that during the interval of data we study, the break most often occurs at $k \simeq k_c$ and not $kd_i \simeq 1$ or $k\rho_i \simeq 1$, as clearly shown during periods where $\beta_{i,\perp} \sim 1$. This result is consistent with studies of turbulence at

extreme $\beta_{i,\perp}$ (e.g., Smith et al. 2001; Chen et al. 2014). In their study, Chen et al. (2014) rule out the role of k_c since they assume $k_{\perp} \gg k_{\parallel}$ at ion-kinetic scales. However, other studies show that the k_{\parallel} component of the turbulence, while small compared to k_{\perp} , increases around ion-kinetic scales (Bieber et al. 1996; Leamon et al. 1998b; Dasso et al. 2005; Hamilton et al. 2008; Roberts & Li 2015). Our results suggest that this small k_{\parallel} component of the turbulence is damped from the cascade, which leads to the observed spectral steepening at these scales.

We note that previous studies (e.g., Markovskii et al. 2008; Bourouaine et al. 2012; Bruno & Trenchi 2014; Chen et al. 2014) include an additional $\sin \theta_{Bv}$ factor in the definition of the associated break scales in order to account for the anisotropic nature of the turbulence at kinetic scales, where θ_{Bv} is the angle between the magnetic field, \mathbf{B} , and velocity flow, v_{sw} . The inclusion of this factor in our analysis only slightly improves our correlations and lowers our residuals by about 10% for f_{di} and f_{ρ_i} . Therefore, it is not necessary to include this factor since the agreement of f_{kc} with f_b or f_h is still clearly better than the agreement of $f_{di} \sin \theta_{Bv}$ and $f_{\rho_i} \sin \theta_{Bv}$, showing that we cannot rule out cyclotron damping because of the anisotropy of inertial range turbulence.

Recent studies by Markovskii et al. (2015, 2016) and Markovskii & Vasquez (2016) attribute the coherent helicity signature to two competing processes, one that generates and another that destroys magnetic helicity: the generation of helicity is due to the increased compressional component of KAW fluctuations at small scales and the development of a magnetic field component parallel to the local mean field (Howes & Quataert 2010; TenBarge & Howes 2012; Markovskii & Vasquez 2013a, 2013b), whereas the decrease in helicity arises from the demagnetization of the protons from the magnetic field (Vasquez & Markovskii 2012). Markovskii et al. (2015) interpret the peak in the helicity as arising from the balance of these two processes. In a later study, Markovskii et al. (2016) find that this peak is best correlated with the gyroscale modified by the electron beta, β_e : $\rho_i = d_i / \sqrt{\beta_i + \beta_e}$, and is therefore affected by the total plasma pressure. We do not use electron data here; however, if $\beta_i = \beta_e$, then β_e will contribute a maximum factor of $1/\sqrt{2}$, roughly equivalent to the uncertainty in our results from the use of a Morlet wavelet. We see that the coherent helicity signature disappears toward smaller scales than ρ_i . Therefore, no significant difference in our results should arise from excluding electron data.

We cannot rule out that a combination of processes may lead to the observed helicity signature, for example, from the increased compressional component of KAWs (e.g., Howes & Quataert 2010) or from the presence of magnetosonic/whistler waves (Podesta & Gary 2011a, 2011b). However, our results suggest the dominant cause of the onset of the observed signature is proton cyclotron resonance with AICs. We do not investigate the origin of these cyclotron resonant fluctuations, but rather show evidence for their existence and subsequent dissipation. We also see that the coherent helicity signature disappears toward smaller scales than ρ_i . The disappearance of the signature at higher frequencies may be due to the demagnetization of protons (Vasquez & Markovskii 2012), the increasing balance of sunward and anti-sunward energy fluxes at smaller scales (He et al. 2012b), aliasing of power (Russell 1972; Klein et al. 2014), or instrumental noise. We are

unable to determine the cause of the return of σ_m to around zero from this study.

Our results also indicate that the transition range often observed in fast wind streams, which follows a break in the power spectrum of the magnetic field fluctuations at ion-kinetic scales, may result from proton cyclotron resonance. This link is consistent with the findings of several other studies (Podesta 2009; Bourouaine et al. 2010; Bruno et al. 2014; Bruno & Telloni 2015; Roberts et al. 2017). We note that our results do not rule out the role of other nonlinear wave-particle interactions and kinetic non-resonant mechanisms resulting in dissipation or the onset of dispersive effects. In fact, past studies by Leamon et al. (1998a, 1998b, 1999, 2000) and Smith et al. (2012) have shown that non-resonant damping (e.g., Landau or transit-time damping) of ions and electrons likely accounts for the remaining $\sim 50\%$ of dissipation, which is consistent with our findings that cyclotron resonant damping is occurring 52.13% of the time.

4. Summary and Conclusions

We use magnetic field and particle moment data from the MFI and SWE instruments on board the *Wind* spacecraft to study the nature of the solar wind turbulence at ion-kinetic scales. We first analyze solar wind data from 2012, investigating the spectral properties of the magnetic field. We use a Morlet continuous wavelet transform to compute the power and normalized magnetic helicity spectra for successive 92 s intervals. To determine whether spectral features are physical at high frequencies, we identify the noise-floor of the MFI instrument using tail-lobe crossings of the Earth's magnetosphere from early 2004, finding it at a higher amplitude than originally predicted. Finally, we use particle data at the same 92 s cadence to calculate the characteristic proton scales, $1/k_c$, d_i , and ρ_i , and investigate their relationship with the spectral break and coherent helicity signature at ion-kinetic scales.

Our automated routine to analyze power and helicity spectra of the solar wind magnetic field combines both the identification of the break scale and analysis of the properties of the magnetic fluctuations at ion-kinetic scales. This analysis of high-resolution spectra accounts for the variability of the plasma scales under different solar wind conditions, while also processing large volumes of solar wind data. For the first time, we link the spectral break frequency, helicity onset, and cyclotron resonance scale. We expand on past results by investigating both fast and slow wind streams, as well as periods where $\beta_{i,\perp} \sim 1$.

In agreement with Bruno & Trenchi (2014), Bruno & Telloni (2015), and Telloni et al. (2015), we find that the high-frequency spectral steepening in a fast wind stream is best associated with the cyclotron resonance scale, $1/k_c$, which also forms the low-frequency bound of a coherent helicity signature. We show for the first time that this result holds in general for fast streams and to a lesser extent for slow wind, where the helicity signature weakens or disappears completely. We also find that the peak of the helicity enhancement is associated with the ion gyroscale, ρ_i , consistent with the findings of Markovskii et al. (2015), again best seen within fast streams, where the enhancement in σ_m is strongest.

Our key result presented here is evidence supporting proton cyclotron resonant damping as a dissipation mechanism of solar wind turbulence at ion-kinetic scales, occurring at least half the time in the solar wind. This resonance results in the

damping of Alfvén/ion-cyclotron waves, particularly in the more Alfvénic fast wind, leading to the steepening of the power spectrum of magnetic field fluctuations. Therefore, we suggest that the AICs are removed from the turbulence at these scales, resulting in a coherent helicity spectrum from the remaining KAWs, which are not cyclotron resonant with protons. We note that we do not speculate about the origin of the cyclotron resonant fluctuations, but rather show evidence for their existence and dissipation.

Further investigative work is on-going to determine the relative importance of proton cyclotron resonance for the dissipation of turbulence and subsequent heating of the particle distributions. In particular, we still need to quantify the energy dissipated and the amount of energy that continues to cascade down to electron scales. We leave this work to a subsequent study. Understanding the nature of dissipation of the turbulence in the solar wind will provide us with a deeper understanding of the macroscopic properties of the solar wind and insight into similar processes in other collisionless plasmas. The future *Solar Orbiter* and *Parker Solar Probe* missions will also help us to explore these important areas of heliophysics research.

L.D.W. is funded by an STFC Studentship; D.V. is supported by an STFC Ernest Rutherford Fellowship, ST/P003826/1; C.J.O. is supported by the STFC consolidated grant to UCL/MSSL, ST/N000722/1. The authors thank R.L. Alexander for providing suitable intervals for our noise-floor analysis and the MFI/SWE instrument teams for provision of the data. The authors also acknowledge A.R. Macneil, G.A. Graham, N.M.E. Kalmoni, O.W. Roberts, C.H.K. Chen, and H. Wu for useful comments and discussions. Data from the *Wind* spacecraft were obtained from the SPDF website.⁴

Appendix Determination of the MFI Noise-floor

The trajectory of the *Wind* spacecraft allows us to determine the noise-floor of the MFI instrument using in situ data. To measure the noise level at high frequencies, we require measurements of “quiet,” smoothly varying magnetic field so that there are as few physical fluctuations as possible at these frequencies and noise completely dominates the measured signal. The solar wind is largely unsuitable for this due to the presence of broadband turbulent fluctuations. However, the spacecraft spent considerable time in the Earth’s magnetosphere before 2005. In particular, during early 2004, *Wind* made several passes through the tail-lobes of the far magnetotail. These high-latitude regions surrounding the central plasma sheet have characteristic low plasma density and stretched-out field lines, and so there are few high-frequency fluctuations in the field.

The MFI instrument has several dynamic range-gates, which are used to measure the components of the magnetic field vector within a specific range of values; the default is ± 16 nT (Lepping et al. 1995). When one of the field components exceeds an amplitude of 14 nT, there is a transition to the next gate, ± 64 nT. It is likely that the noise level at high frequencies has a different amplitude for each range-gate since the digital resolution decreases by a factor of 4 for each consecutive range-gate. This effect should increase the noise level by a factor of about 2 for each gate. Despite this, we consider the noise-floor only for the

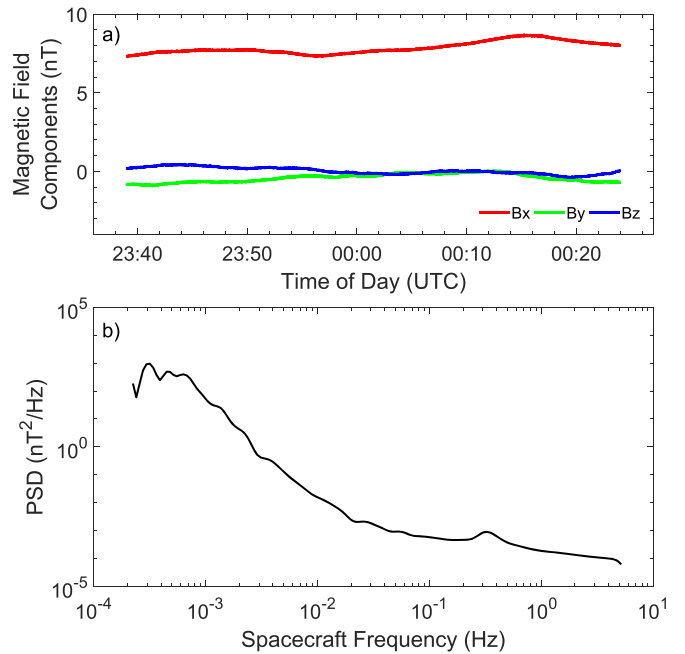


Figure 10. (a) Magnetic field components in GSE coordinates from one of our selected intervals for determining the noise-floor (23:39-00:24, 2004 February 12–13). (b) The corresponding PSD of the trace power spectrum of the magnetic field for the same interval, highlighting the flattening of the spectrum at high frequencies due to noise, as well as the peak at about 0.33 Hz due to spacecraft spin.

default range-gate, ± 16 nT, since the magnetic field components typically do not exceed ± 14 nT during quiet conditions in the solar wind. In the rare instance that the magnetic field exceeds this threshold, we use a conservative S/N of 10 that should minimize any impact on our results.

Using the criteria we have discussed, we identify 89 suitable tail-lobe intervals to determine the noise-floor. We show the time series of the magnetic field from an example interval from early 2004 February in Figure 10(a), and its corresponding power spectrum in Figure 10(b), revealing the noise-floor at high frequencies and illustrating the quietness of our selected period. To find the instrument noise level, we calculate the PSD using Equation (8) and average over each interval, using the method documented in Section 2.1, padding each interval to remove any border effects. All identified periods are between 30 minutes and several hours, long enough to provide a stable estimate of the PSD. We refine the selected intervals down to a final 22 periods by removing data sets with signals attributed to physical fluctuations above 0.1 Hz and average the PSD estimates for all intervals together to give one final estimate for the noise-floor. We show the PSD for all 22 periods in Figure 11. In addition, the black line shows the average and the red line the original noise-floor estimate published by Lepping et al. (1995), performed on a prototype sensor before launch.

The major difference in our noise-floor spectrum compared with the original estimate is the peak at 0.33 Hz. We attribute this peak to the spin of the spacecraft every 3 s. This peak is notch-filtered as described by Koval & Szabo (2013) to remove most of this artifact, but some residual power remains. At frequencies higher than the peak, we find a power-law fit of $\text{PSD} = af^b$ where $a = 1.944 \times 10^{-4}$ and $b = -0.5328$, before the amplitude eventually coincides with the original estimate at about 3 Hz. This high-frequency part of the spectrum is due to the aliasing of the spin-tone harmonics

⁴ <http://spdf.gsfc.nasa.gov>

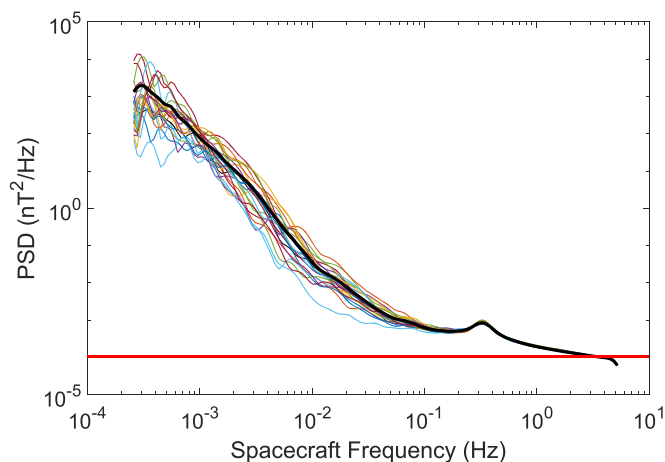


Figure 11. PSD of the final 22 data sets used for the combined estimate of the average MFI noise-floor, given by the black line. The red line is the original determination by Lepping et al. (1995). The data used to create this figure are available.

(Koval & Szabo 2013), which cannot be removed by filtering, as well as noise from the digitization process (Bennett 1948; Russell 1972). Another source of noise is the aliasing of power due to the presence of turbulent fluctuations measured at frequencies higher than the Nyquist frequency (5.4 Hz) of the MFI instrument (Russell 1972; Klein et al. 2014). This effect cannot be completely removed by our noise-floor treatment here; however, our estimate works well with solar wind data. Approaching the Nyquist frequency, the spectrum steepens again, but this is due to effects of the wavelet transform. We take the amplitude of power at frequencies <0.1 Hz as being due to physical fluctuations in the magnetic field and not instrument- or spacecraft-induced noise.

Although not shown here, we also identified intervals from 2000–2003 to calculate the noise-floor, but these show no substantial variation in the noise level compared to the results from 2004. The differences between our noise-floor estimate and the original estimate by Lepping et al. (1995) show that the noise level in the range 0.1–1 Hz is greater than initially thought, highlighting its importance when investigating turbulent phenomena in the solar wind at these frequencies. We use the amplitude of the PSD between 0.1 and 5.4 Hz as the noise-floor in our analysis of the turbulent magnetic field fluctuations in the solar wind, incorporating both the peak due to spacecraft spin and the high-frequency power-law component. We provide our data set of the noise-floor at these frequencies as data behind Figure 11 for use in future studies.

ORCID iDs

Lloyd D. Woodham <https://orcid.org/0000-0003-2845-4250>

Robert T. Wicks <https://orcid.org/0000-0002-0622-5302>

Daniel Verscharen <https://orcid.org/0000-0002-0497-1096>

Christopher J. Owen <https://orcid.org/0000-0002-5982-4667>

References

Acuña, M. H., Ogilvie, K. W., Baker, D. N., et al. 1995, *SSRv*, 71, 5
 Alexandrova, O., Chen, C. H. K., Sorriso-Valvo, L., Horbury, T. S., & Bale, S. D. 2013, *SSRv*, 178, 101

- Bale, S. D., Kasper, J. C., Howes, G. G., et al. 2009, *PhRvL*, 103, 211101
 Batchelor, G. K. 1970, *The Theory of Homogenous Turbulence* (Cambridge: Cambridge Univ. Press)
 Bennett, W. R. 1948, *Bell Syst. Tech. J.*, 27, 446
 Bieber, J. W., Wanner, W., & Matthaeus, W. H. 1996, *JGRA*, 101, 2511
 Boldyrev, S., Horaites, K., Xia, Q., & Perez, J. C. 2013, *ApJ*, 777, 41
 Boldyrev, S., & Perez, J. C. 2012, *ApJL*, 758, L44
 Bourouaine, S., Alexandrova, O., Marsch, E., & Maksimovic, M. 2012, *ApJ*, 749, 102
 Bourouaine, S., Marsch, E., & Neubauer, F. M. 2010, *GeoRL*, 37, L14104
 Brandenburg, A., Subramanian, K., Balogh, A., & Goldstein, M. L. 2011, *ApJ*, 734, 9
 Bruno, R., & Carbone, V. 2013, *LRSP*, 10, 2
 Bruno, R., & Telloni, D. 2015, *ApJL*, 811, L17
 Bruno, R., Telloni, D., Delure, D., & Pietropaolo, E. 2017, *MNRAS*, 472, 1052
 Bruno, R., & Trenchi, L. 2014, *ApJL*, 787, L24
 Bruno, R., Trenchi, L., & Telloni, D. 2014, *ApJL*, 793, L15
 Cerri, S. S., Califano, F., Jenko, F., Told, D., & Rincon, F. 2016, *ApJL*, 822, L12
 Chandran, B. D. G., Li, B., Rogers, B. N., Quataert, E., & Germaschewski, K. 2010, *ApJ*, 720, 503
 Chen, C. H. K. 2016, *JPIPh*, 82, 535820602
 Chen, C. H. K., Horbury, T. S., Schekochihin, A. A., et al. 2010a, *PhRvL*, 104, 255002
 Chen, C. H. K., Leung, L., Boldyrev, S., Maruca, B. A., & Bale, S. D. 2014, *GeoRL*, 41, 8081
 Chen, C. H. K., Wicks, R. T., Horbury, T. S., & Schekochihin, A. A. 2010b, *ApJL*, 711, L79
 Coleman, P. J., Jr. 1968, *ApJ*, 153, 371
 Cranmer, S. R., Matthaeus, W. H., Breech, B. A., & Kasper, J. C. 2009, *ApJ*, 702, 1604
 Dasso, S., Milano, L. J., Matthaeus, W. H., & Smith, C. W. 2005, *ApJL*, 635, L181
 Denskat, K. U., Beinroth, H. J., & Neubauer, F. M. 1983, *JGZG*, 54, 60
 Dmitruk, P., Matthaeus, W. H., & Seenu, N. 2004, *ApJ*, 617, 667
 Forman, M. A., Wicks, R. T., & Horbury, T. S. 2011, *ApJ*, 733, 76
 Franci, L., Cerri, S. S., Califano, F., et al. 2017, *ApJL*, 850, L16
 Franci, L., Landi, S., Matteini, L., Verdini, A., & Hellinger, P. 2016, *ApJ*, 833, 91
 Galtier, S. 2006, *JPIPh*, 72, 721
 Galtier, S., & Buchlin, E. 2007, *ApJ*, 656, 560
 Gary, S. P. 1986, *JPIPh*, 35, 431
 Gary, S. P. 1993, *Theory of Space Plasma Microinstabilities* (Cambridge: Cambridge Univ. Press)
 Gary, S. P. 1999, *JGRA*, 104, 6759
 Gary, S. P. 2015, *RSPTA*, 373, 20140149
 Gary, S. P., & Borovsky, J. E. 2004, *JGRA*, 109, A06105
 Gary, S. P., & Smith, C. W. 2009, *JGRA*, 114, A12105
 Ghosh, S., Siregar, E., Roberts, D. A., & Goldstein, M. L. 1996, *JGRA*, 101, 2493
 Goldstein, M. L., Roberts, D. A., & Fitch, C. A. 1994, *JGRA*, 99, 11519
 Goldstein, M. L., Roberts, D. A., & Matthaeus, W. H. 1995, *ARA&A*, 33, 283
 Habbal, S. R., Woo, R., Fineschi, S., et al. 1997, *ApJL*, 489, L103
 Hamilton, K., Smith, C. W., Vasquez, B. J., & Leamon, R. J. 2008, *JGRA*, 113, A01106
 He, J., Marsch, E., Tu, C. Y., Yao, S., & Tian, H. 2011, *ApJ*, 731, 85
 He, J., Tu, C. Y., Marsch, E., et al. 2015a, *ApJL*, 813, L30
 He, J., Tu, C. Y., Marsch, E., & Yao, S. 2012a, *ApJL*, 745, L8
 He, J., Tu, C. Y., Marsch, E., & Yao, S. 2012b, *ApJ*, 749, 86
 He, J., Wang, L., Tu, C. Y., Marsch, E., & Zong, Q. 2015b, *ApJL*, 800, L31
 Hellinger, P., Trávníček, P. M., Kasper, J. C., & Lazarus, A. J. 2006, *GeoRL*, 33, L09101
 Heuer, M., & Marsch, E. 2007, *JGRA*, 112, A03102
 Horbury, T. S., Forman, M. A., & Oughton, S. 2008, *PhRvL*, 101, 175005
 Howes, G. G., Cowley, S. C., Dorland, W., et al. 2008a, *JGRA*, 113, A05103
 Howes, G. G., Dorland, W., Cowley, S. C., et al. 2008b, *PhRvL*, 100, 065004
 Howes, G. G., & Quataert, E. 2010, *ApJL*, 709, L49
 Jian, L. K., Russell, C. T., Luhmann, J. G., et al. 2009, *ApJL*, 701, L105
 Jian, L. K., Russell, C. T., Luhmann, J. G., et al. 2010, *JGRA*, 115, A12115
 Jian, L. K., Wei, H. Y., Russell, C. T., et al. 2014, *ApJ*, 786, 123
 Kasper, J. C., Lazarus, A. J., & Gary, S. P. 2002, *GeoRL*, 29, 1839
 Kiyani, K. H., Chapman, S. C., Khotyaintsev, Y. V., Dunlop, M. W., & Sahraoui, F. 2009, *PhRvL*, 103, 075006
 Kiyani, K. H., Chapman, S. C., Sahraoui, F., et al. 2013, *ApJ*, 763, 10
 Kiyani, K. H., Osman, K. T., & Chapman, S. C. 2015, *RSPTA*, 373, 20140155
 Klein, K. G., Howes, G. G., TenBarge, J. M., & Podesta, J. J. 2014, *ApJ*, 785, 138

- Koval, A., & Szabo, A. 2013, in AIP Conf. Proc. 1539, SOLAR WIND 13, ed. G. P. Zank et al. (Melville, NY: AIP), 211
- Leamon, R. J., Matthaeus, W. H., Smith, C. W., et al. 2000, *ApJ*, 537, 1054
- Leamon, R. J., Matthaeus, W. H., Smith, C. W., & Wong, H. K. 1998a, *ApJL*, 507, L181
- Leamon, R. J., Smith, C. W., Ness, N. F., Matthaeus, W. H., & Wong, H. K. 1998b, *JGRA*, 103, 4775
- Leamon, R. J., Smith, C. W., Ness, N. F., & Wong, H. K. 1999, *JGRA*, 104, 22331
- Lepping, R. P., Acuña, M. H., Burlaga, L. F., et al. 1995, *SSRv*, 71, 207
- Lion, S., Alexandrova, O., & Zaslavsky, A. 2016, *ApJ*, 824, 47
- MacBride, B. T., Smith, C. W., & Forman, M. A. 2008, *ApJ*, 679, 1644
- Markovskii, S. A., & Vasquez, B. J. 2013a, *ApJ*, 768, 62
- Markovskii, S. A., & Vasquez, B. J. 2013b, in AIP Conf. Proc. 1539, SOLAR WIND 13, ed. G. P. Zank et al. (Melville, NY: AIP), 239
- Markovskii, S. A., & Vasquez, B. J. 2016, *ApJ*, 820, 15
- Markovskii, S. A., Vasquez, B. J., & Smith, C. W. 2008, *ApJ*, 675, 1576
- Markovskii, S. A., Vasquez, B. J., & Smith, C. W. 2015, *ApJ*, 806, 78
- Markovskii, S. A., Vasquez, B. J., & Smith, C. W. 2016, *ApJ*, 833, 212
- Marsch, E. 2006, *LRSP*, 3, 1
- Marsch, E. 2012, *SSRv*, 172, 23
- Marsch, E., Ao, X. Z., & Tu, C. Y. 2004, *JGRA*, 109, A04102
- Marsch, E., Goertz, C. K., & Richter, K. 1982a, *JGRA*, 87, 5030
- Marsch, E., Mühlhäuser, K. H., Schwenn, R., et al. 1982b, *JGRA*, 87, 52
- Marsch, E., & Tu, C. Y. 2001, *JGRA*, 106, 8357
- Marsch, E., Vocks, C., & Tu, C. Y. 2003, *NPGeo*, 10, 101
- Maruca, B. A., & Kasper, J. C. 2013, *AdSpR*, 52, 723
- Maruca, B. A., Kasper, J. C., & Gary, S. P. 2012, *ApJ*, 748, 137
- Matteini, L., Landi, S., Hellinger, P., et al. 2007, *GeoRL*, 34, L20105
- Matthaeus, W. H., & Goldstein, M. L. 1982a, *JGRA*, 87, 6011
- Matthaeus, W. H., & Goldstein, M. L. 1982b, *JGRA*, 87, 10347
- Matthaeus, W. H., Goldstein, M. L., & Smith, C. W. 1982, *PhRvL*, 48, 1256
- Moffat, H. K. 1978, *Magnetic Field Generation in Electrically Conducting Fluids* (Cambridge: Cambridge Univ. Press)
- Montgomery, M. D., & Turner, L. 1981, *PhFI*, 24, 825
- Ogilvie, K. W., Chornay, D. J., Fritzenreiter, R. J., et al. 1995, *SSRv*, 71, 55
- Osman, K. T., Matthaeus, W. H., Gosling, J. T., et al. 2014, *PhRvL*, 112, 215002
- Osman, K. T., Matthaeus, W. H., Kiyani, K. H., Hnat, B., & Chapman, S. C. 2013, *PhRvL*, 111, 201101
- Perri, S., & Balogh, A. 2010, *ApJ*, 714, 937
- Perri, S., Carbone, V., & Veltri, P. 2010, *ApJL*, 725, L52
- Perri, S., Goldstein, M. L., Dorelli, J. C., & Sahraoui, F. 2012, *PhRvL*, 109, 191101
- Podesta, J. J. 2009, *ApJ*, 698, 986
- Podesta, J. J., & Gary, S. P. 2011a, *ApJ*, 742, 41
- Podesta, J. J., & Gary, S. P. 2011b, *ApJ*, 734, 15
- Richardson, J. D., Paularena, K. I., Lazarus, A. J., & Belcher, J. W. 1995, *GeoRL*, 22, 325
- Roberts, O. W., & Li, X. 2015, *ApJ*, 802, 1
- Roberts, O. W., Li, X., & Jeska, L. 2015, *ApJ*, 802, 2
- Roberts, O. W., Narita, Y., & Escoubet, C. P. 2017, *ApJL*, 851, L11
- Russell, C. T. 1972, *NASSP*, 308, 365
- Sahraoui, F., Goldstein, M. L., Belmont, G., Canu, P., & Rezeau, L. 2010, *PhRvL*, 105, 131101
- Schekochihin, A. A., Cowley, S. C., Dorland, W., et al. 2009, *ApJS*, 182, 310
- Schwenn, R. 1990, in *Physics of the Inner Heliosphere I*, ed. R. Schewenn & E. Marsch (Berlin: Springer), 99
- Servidio, S., Osman, K. T., Valentini, F., et al. 2014, *ApJL*, 781, L27
- Smith, C. W. 2003, *AdSpR*, 32, 1971
- Smith, C. W., Hamilton, K., Vasquez, B. J., & Leamon, R. J. 2006, *ApJL*, 645, L85
- Smith, C. W., Matthaeus, W. H., Zank, G. P., et al. 2001, *JGRA*, 106, 8253
- Smith, C. W., Vasquez, B. J., & Hollweg, J. V. 2012, *ApJ*, 745, 8
- Stawarz, J. E., Smith, C. W., Vasquez, B. J., Forman, M. A., & MacBride, B. T. 2009, *ApJ*, 697, 1119
- Stix, T. H. 1992, *Waves in Plasmas* (Melville, NY: AIP)
- Taylor, G. I. 1938, *RSPSA*, 164, 476
- Telloni, D., & Bruno, R. 2016, *MNRAS*, 463, L79
- Telloni, D., Bruno, R., D'Amicis, R., Pietropaolo, E., & Carbone, V. 2012, *ApJ*, 751, 19
- Telloni, D., Bruno, R., & Trenchi, L. 2015, *ApJ*, 805, 46
- Telloni, D., Perri, S., Bruno, R., Carbone, V., & D'Amicis, R. 2013, *ApJ*, 776, 3
- TenBarge, J. M., & Howes, G. G. 2012, *PhPI*, 19, 055901
- TenBarge, J. M., Podesta, J. J., Klein, K. G., & Howes, G. G. 2012, *ApJ*, 753, 107
- Torrence, C., & Compo, G. P. 1998, *BAMS*, 79, 61
- Tsurutani, B. T., Arballo, J. K., Mok, J., et al. 1994, *GeoRL*, 21, 633
- Tu, C. Y., & Marsch, E. 1995, *SSRv*, 73, 1
- Tu, C. Y., & Marsch, E. 2001, *JGRA*, 106, 8233
- Tu, C. Y., & Marsch, E. 2002, *JGRA*, 107, 1249
- Vasquez, B. J., & Markovskii, S. A. 2012, *ApJ*, 747, 19
- Wang, X., Tu, C. Y., He, J., & Wang, L.-H. 2018, *JGRA*, 123, 68
- Wicks, R. T., Alexander, R. L., Stevens, M. L., et al. 2016, *ApJ*, 819, 6
- Wicks, R. T., Forman, M. A., Horbury, T. S., & Oughton, S. 2012, *ApJ*, 746, 103
- Wicks, R. T., Horbury, T. S., Chen, C. H. K., & Schekochihin, A. A. 2010, *MNRAS*, 407, L31
- Woltjer, L. 1958, *PNAS*, 44, 489